Bioinsp. Biomim. **6** (2011) 026005 (20pp) doi:10.1088/1748-3182/6/2/026005

Flight mechanics of a tailless articulated wing aircraft

Aditya A Paranjape, Soon-Jo Chung and Michael S Selig

Department of Aerospace Engineering, University of Illinois at Urbana-Champaign, Urbana, IL 61801, USA

E-mail: sjchung@illinois.edu

Received 22 October 2010
Accepted for publication 16 March 2011
Published 12 April 2011
Online at stacks.iop.org/BB/6/026005

Abstract
This paper investigates the flight mechanics of a micro aerial vehicle without a vertical tail in an effort to reverse-engineer the agility of avian flight. The key to stability and control of such a tailless aircraft lies in the ability to control the incidence angles and dihedral angles of both wings independently. The dihedral angles can be varied symmetrically on both wings to control aircraft speed independently of the angle of attack and flight path angle, while asymmetric dihedral can be used to control yaw in the absence of a vertical stabilizer. It is shown that wing dihedral angles alone can effectively regulate sideslip during rapid turns and generate a wide range of equilibrium turn rates while maintaining a constant flight speed and regulating sideslip. Numerical continuation and bifurcation analysis are used to compute trim states and assess their stability. This paper lays the foundation for design and stability analysis of a flapping wing aircraft that can switch rapidly from flapping to gliding flight for agile manoeuvring in a constrained environment.

(Some figures in this article are in colour only in the electronic version)

1. Introduction

There is an increasing interest in the aerospace community to learn and mimic avian flight with the ultimate objective of designing unmanned aerial vehicles which are autonomous, agile and capable of flying in constrained environments [1]. Birds are natural role models for designing micro air vehicles (MAVs) wherein the aforementioned attributes can be engineered. MAVs typically fly in a low Reynolds number range of 10^3–10^5 [2] which coincides with that of birds. Therefore, it is worth investigating the mechanics of avian flight and making an attempt to reverse-engineer them. Conversely, a study of the flight mechanics of MAVs can shed light on several aspects of bird flight.

This paper contributes to the broader problem of developing a flapping MAV capable of agile flight in constrained environments. Chung and Dorothy [3] studied a neurobiologically inspired controller for flapping flight, and demonstrated it on a robotic testbed. Their controller could switch in a stable and smooth fashion between flapping and gliding flight. Among other phases of flight, gliding is essential during landing and perching. This paper provides the analytical foundations needed to design effective gliding and landing strategies.

The objective of this paper is to describe a novel bioinspired concept for MAVs. It is based on the observation that birds lack a vertical tail, and they use their wings effectively for control. Wing dihedral and incidence angles are controlled actively as birds execute agile and even spatially constrained manoeuvres. Complex manoeuvres require a combination of open and closed loop capabilities. However, the performance achievable in the closed loop (with control and guidance) is contingent upon the limitations of the airframe. The focus of this paper is on the airframe (open loop) rather than feedback control.

The tailless aircraft in this paper has rigid wings each of which can be rotated at the root to generate variable incidence and dihedral. The dihedral and incidence angles on both wings need not be equal. The concept of asymmetric dihedral is used to explore yaw stability and control in the absence of a vertical tail. Table 1 lists the symbols used in the paper.

 © 2011 IOP Publishing Ltd Printed in the UK

Table 1. List of symbols.

Symbol	Meaning
C_L, C_D	coefficients of lift and drag
D, Y	drag and side force
$\mathbf{F}, \mathbf{M}$	force and moment vectors
$\mathbf{J}_{R,R}, \mathbf{J}_{L,L}$	moment of inertia tensor of the right and left wings in their respective wing root frames
$\mathbf{J}_R, \mathbf{J}_L, \mathbf{J}$	moment of inertia tensor of the right and left wings, and the aircraft body in the aircraft body frame
L, M, N	body axis rolling, pitching and yawing moments
L_β	$\frac{\partial L}{\partial \beta}$; $L_p, L_r, N_\beta, N_p, N_r$ defined similarly
l_w, l_t	longitudinal distance of the wing and tail aerodynamic centres from the body frame origin
m_w, m	mass of each wing, and mass of the aircraft
p, q, r	body axis roll, pitch, and yaw rates
$\mathbf{r}_{CG}$	position vector of the aircraft centre of gravity
S_w, S_t	area of each wing, and area of vertical tail
u, v, w	body axis aircraft wind velocity components
$\mathbf{u}_B$	aircraft velocity vector with components in the body frame
$\mathbf{V}$	local wind velocity vector
X, Y, Z	x-, y-, and z-component of force
α, β	angle of attack and sideslip angle
β_L, β_R	left- and right-wing sweep
γ, χ	flight path angle and wind heading angle
δ_e	elevator or horizontal tail deflection
δ_L, δ_R	dihedral angle of left and right wing
ζ	dihedral effectiveness ratio
ϕ, θ, ψ	Euler angles
θ_L, θ_R	left- and right-wing incidence
θ_a	anti-symmetric wing incidence, $\theta_R = -\theta_L = -\theta_a$
ω	turn rate
$\boldsymbol{\omega}_{\{\}}$	angular velocity vector (see subscripts)
Subscripts	
B	aircraft body
L, R	left and right wing, respectively

1.1. Literature review

The idea of using cant-angle winglets for control was investigated experimentally by Bourdin, Gatto and Friswell [4, 5] for larger aircraft operating at high Reynolds numbers. On the other hand, this paper is focussed on MAVs flying at low Reynolds number, and the analysis presented herein is theoretical and computational in nature. The restriction to MAVs comes from two factors. First, the articulated wing-based mechanism proposed in this paper would be impractical for larger aircraft. Second, the low flight speeds considered here are characteristic of MAVs. Low flight speeds imply that the local angle of attack distribution on the wing is a nonlinear function of the angular velocity of the aircraft. The nonlinearity manifests itself in, for example, the peculiar relation between the turn rate and the commanded dihedral as described later in this paper.

Fixed and flapping wing MAVs have been extensively studied in the literature. The reader is referred to an excellent compendium of papers [2] which showcases some of the work done in this area until circa 2000. More recently, Costello and Webb [6] demonstrated that articulated wing MAVs, with wings hinged at the root, experience reduced gust sensitivity. Wickenheiser and Garcia [7, 8] studied the dynamics of morphing aircraft and demonstrated perching using, among other forms of articulation, variable wing incidence. Reich *et al* [9] experimentally studied the aerodynamic performance of a wing of variable incidence for perching.

Stenfelt and Ringertz [10, 11] studied the stability and control of tailless aircraft equipped with a split flap mechanism, while Shtessel, Buffington and Banda [12] designed a sliding mode-based controller for tailless fighter aircraft. Recently, Obradovic and Subbarao [13] investigated the power requirement for morphing, and used it as a basis to compare wing morphing and the traditional aileron-based control in different flight regimes.

The lateral stability and control of birds, and in particular, the role of wing dihedral, have been studied extensively by Sachs and co-authors [14–16]. Sachs has demonstrated that for air vehicles whose size and speed (and hence, Reynolds number) are similar to those of birds, wings are sufficient to provide lateral stability thereby reducing, if not eliminating altogether, the need for a vertical tail. Tran and Lind [17] have studied numerically the stability of an aircraft equipped with variable symmetric dihedral and incidence.

1.2. Main contributions

At a conceptual level, this paper is a study of yaw control using asymmetric dihedral, a concept which was put forth by Bourdin, Gatto and Friswell [4] along with detailed moment calculations as well as elementary trim analysis. In contrast with the earlier work, this paper is dedicated to MAVs whose speed and size, and resultant low Reynolds numbers (10^3–10^5), present several distinct characteristics from the point of view of control and even stability. The small size of MAV wings makes wing articulation practically feasible. Unlike conventional fixed wing aircraft, an articulated wing aircraft changes its configuration routinely and therefore, stability is closely tied to the nature of the manoeuvre being executed. Another feature of this work is the extensive use of bifurcation analysis [18–20] to explore the dynamics of tailless aircraft equipped with articulated wings. As demonstrated in this paper, bifurcation analysis not only measures the stability characteristics of the aircraft but also helps predict the performance limitations that arise because of the use of asymmetric dihedral.

Furthermore, this paper includes detailed theoretical and linear computational analyses of the lateral dynamics. Longitudinal dynamics are not affected by the absence of a vertical stabilizer. Analytical expressions for lateral-directional aerodynamic force and moment derivatives offer a valuable insight into the manoeuvre dependence of stability and help identify the source of lateral-directional instability, which is subsequently verified computationally. The analytical expressions also help identify potentially dangerous situations where the control effectiveness of the dihedral may switch sign in the midst of certain manoeuvres. This can not only stall the manoeuvre but may cause an automatic control system to destabilize the aircraft.

It is known that the wing dihedral angle can be varied to perform slow, steep descents [14, 21]. In this paper,

gliding flight trims have been computed numerically along with their stability for the sake of completeness as well as to identify bounds on longitudinal performance. A knowledge of the longitudinal trims can help formulate landing and perching strategies in spatially constrained environments without resorting to manoeuvres like spin [22] and aid the design of control laws for perching [23].

A nonlinear six degree-of-freedom model incorporating dynamic centre of gravity (CG) variation is derived. It can be used for flapping wing aircraft as well, and it is substantially more complete than flapping models in the literature [3, 24].

Aerodynamic forces on the aircraft wings and the horizontal tail are modelled using strip theory with aerodynamic data from Uhlig [25]. A combination of linear stability theory and bifurcation analysis [20] is used to study the performance and stability of a six degree-of-freedom aircraft model that incorporates the effect of dynamic CG location as a function of the aircraft geometry. Performance metrics of interest are (a) trim angle of attack, velocity, and flight path angle for longitudinal flight assessment, and (b) sideslip angle and turn rate for the lateral-directional motion. Coordinated turns are studied using a modified version of the constrained bifurcation analysis [20, 26].

It is interesting to note the roles played by wing incidence and dihedral in turning flight. Turn rate is observed to be sensitive to wing incidence and dihedral angle alike. It is shown that wing incidence and dihedral can effectively maintain zero sideslip and a large turn rate. However, when steady turn trim states are computed at a constant flight speed, the turning performance is seen to depend almost entirely on the dihedral angles of the two wings, with minor dependence on the wing incidence. The maximum achievable turn rate and stability are sensitive to the commanded flight speed.

The ideas presented in this paper have been validated experimentally. Some results obtained during open-loop experiments have been presented in the paper. During the experiments, the aircraft position was measured directly using a VICON motion capture system consisting of eight 2 MP cameras capable of operating at 200 Hz. Reflective markers attached to the aircraft were used by the VICON system to track the aircraft position and attitude. The VICON system and its role have been illustrated in figure 1. Efforts are underway to perform experiments with aircraft flying in the closed loop with an automatic controller, e.g. see [23].

The paper is organized as follows. The mathematical preliminaries are summarized in section 2. Section 3 derives the dynamical equations for tailless articulated wing aircraft, while section 4 describes the aircraft model used in the subsequent analysis. In section 5, an analytical comparison of differential dihedral and vertical tail vis-à-vis their role as yaw control devices is provided. A linear analysis of lateral stability is performed to provide insights into the lateral modes as well as control effectiveness. A bifurcation analysis is performed to identify symmetric as well as asymmetric flight equilibria and their stability. Section 6 describes the experimental results. Section 7 concludes the paper.

2. Preliminaries

In this section, the methods of trim computation and bifurcation analysis, required in the subsequent analysis, are briefly introduced. The reader is referred to the excellent account by Lowenberg [19] for a tutorial introduction to bifurcation analysis, while [18, 20] review its application to problems in flight dynamics.

Numerical bifurcation analysis has two objectives: (1) to correctly compute the trim states and (2) to identify their stability. A linear analysis is incapable of performing task (1) and therefore, numerical continuation is required. Numerical continuation procedures compute the Jacobian matrix as part of the trim computation process, and therefore, it need not be computed again for stability analysis. Therefore, trim computation and stability analysis can be performed together in a very efficient manner, an advantage which would be lost if one were to resort to a separate linear stability analysis.

Consider a set of ordinary differential equations $\dot{x} = f(x, u, \lambda)$, where $x \in \mathbb{R}^n$ are the states, $u \in \mathbb{R}$ is the control input to be varied, and $\lambda \in \mathbb{R}^p$ are other system parameters. A trim (x^*, u^*) is an equilibrium point of this differential equation, i.e. $f(x^*, u^*, \lambda) = 0$. Given a control u^*, there may exist several trim states (x^*, u^*). All of these trim states may not be of interest. Once a trim state (x_0, u_0) is computed, the Jacobian $\frac{\partial f}{\partial x}$ is computed at that trim state. If it is non-singular, it follows from the implicit function theorem that there exists locally a unique branch of trim states passing through (x_0, u_0). This trim branch is computed using numerical continuation [27].

Suppose that the solutions of the dynamical system are required to satisfy m physical constraints (e.g. zero sideslip), where $m < p$. It is quite possible that $m = 0$, in which case there are no constraints. The dynamical equations are augmented with the constraint equations $g(x, u, \lambda) = 0$, and an auxiliary equation called the pseudo-arc length equation. The vector λ is split into two groups: $\lambda_c \in \mathbb{R}^{m-p}$ and $\lambda_u \in \mathbb{R}^m$. The latter is 'freed' to ensure that the enlarged set of equations defines a well-posed problem. The former is held fixed. A new state vector $z = (x, u, \lambda_u) \in \mathbb{R}^{n+m+1}$ is defined. Given an equilibrium solution $z_0 = (x_0, u_0, \lambda_{u0})$, the function `fsolve` in MATLAB™ is used to compute the next equilibrium solution z of the enlarged set of equations

$$\begin{aligned} f(z, \lambda_c) &= 0 \\ g(z, \lambda_c) &= 0 \\ \boldsymbol{\tau}^{\mathrm{T}}(z - z_0) + u_c &= 0, \end{aligned} \tag{1}$$

where u_c is the step size. The vector $\boldsymbol{\tau}$ satisfies

$$\left[\frac{\partial \mathbf{f}}{\partial \mathbf{z}} \middle| \frac{\partial \mathbf{g}}{\partial \mathbf{z}}\right] \boldsymbol{\tau} = 0. \tag{2}$$

The equilibrium z is then used to compute the next equilibrium point, and this process is iterated to determine the equilibrium surface. The pseudo-arc length equation (1) is critical in order to track the solution curve past points where it turns around on itself such that the tangent to the curve is perpendicular to the continuation parameter axis. Such points are called limit points [27].

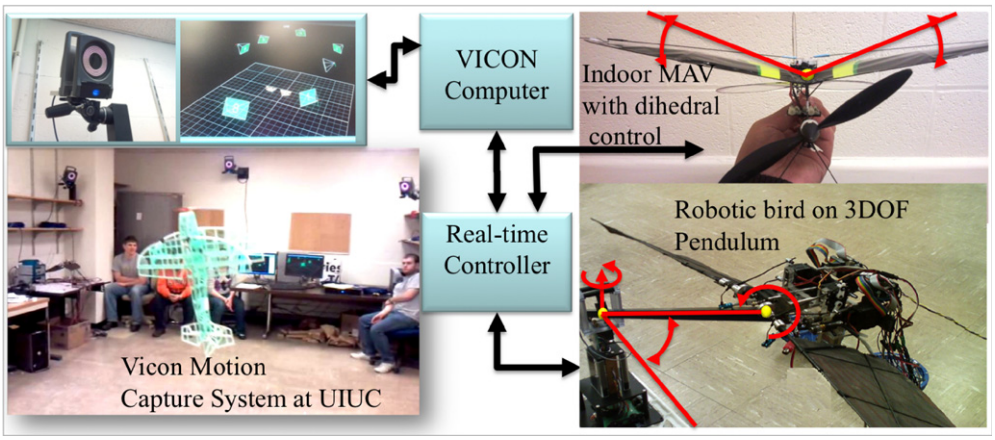

Figure 1. The VICON motion capture system, and its role in analysing and controlling indoor flight.

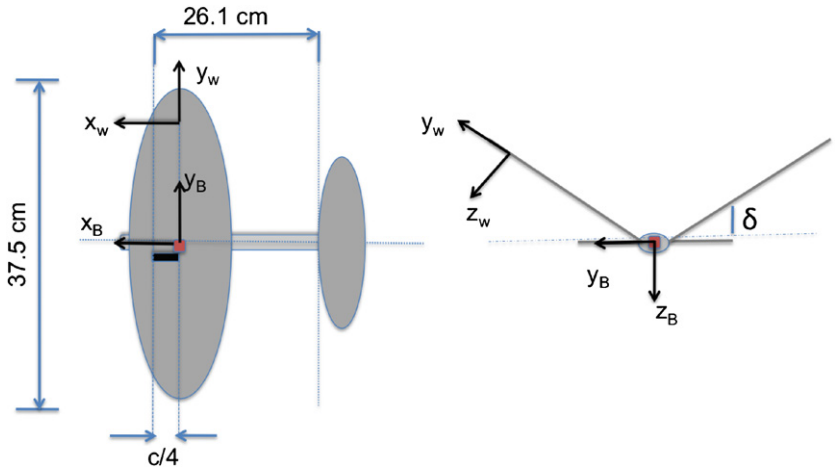

Figure 2. A schematic of the aircraft showing the dimensions and the coordinate systems used to model the aircraft.

The eigenvalues of the Jacobian $\frac{\partial f}{\partial x}$ are used to deduce the stability of a trim point. A trim point at which a trim solution branch undergoes a change in stability is called a bifurcation point. Bifurcations are important not only because they indicate the onset of instability, but also because trim branches or limit cycles originating from the bifurcation point provide indications about the behaviour of the aircraft after it has departed from the unstable trim state. One such bifurcation point is the saddle node bifurcation at which a solution branch 'turns around' in the state space, leading to jumps [20]. Another commonly encountered bifurcation is the Hopf bifurcation which gives rise to limit cycles (or oscillatory behaviour). In this paper, the equilibria computed by the above algorithm are plotted along with a stability-based legend which allows for the identification of bifurcation points. Such plots are called bifurcation diagrams [19].

The algorithm described above is obviously limited in its capabilities. It cannot track limit cycles, perform branch switching or explicitly identify bifurcation points. Despite these limitations, as demonstrated in the paper, this algorithm can provide a wealth of information about the aircraft dynamics. An equilibrium analysis is useful because it helps to locate potential instabilities, identify their nature, and predict the behaviour of the aircraft after departure from the desired trimmed condition should it be unstable. Bifurcation analysis serves as a useful pointer to control design by identifying the basin of attraction of each trim state.

3. Equations of motion for articulated wing aircraft

In this section, the equations of motion for an aircraft with articulated wings have been derived. These equations are complete in that they account for the variations in the CG position as well as the moments of inertia due to wing rotations. These equations can also be used to model the motion of flapping wing aircraft as well.

3.1. Frames of reference

Figure 2 is a schematic diagram of the aircraft along with the dimensions. The x, y, z axes are chosen as per the standard conventions in flight mechanics. The body frame is fixed to the CG, while the wing frame is constructed at every spanwise station of interest. The origin of both frames may accelerate and/or rotate. The moments of inertia are calculated as functions of the dihedral and the incidence angles. The body frame, denoted by B, is attached to the body with the x–z plane coincident with the aircraft plane of symmetry when the wings

are undeflected. The x-axis points towards the aircraft nose. The z-axis points downwards, and the y-axis (pointing along the right undeflected wing) is defined to create a right-handed coordinate system (see figure 2).

Let the matrix $\boldsymbol{T}_{FG}$ denote the rotation matrix which transforms the components of a vector from the G frame to F, where the frames F and G are arbitrary. The frame R is the frame based at the right-wing root. Its x-axis coincides with the x-axis of the B frame and it is related to the B frame via a dihedral rotation δ_R at the wing root followed by a rotation θ_R about the y-axis. The y-axis points along the wing span. Let $\mathbf{R}_1, \mathbf{R}_2, \mathbf{R}_3$ denote the body-to-wing frame rotation matrices for wing rotations about the root hinge corresponding to sweep (β_R), dihedral (δ_R) and incidence (θ_R), respectively. Therefore,

$$\mathbf{R}_1 = \begin{bmatrix} \cos\beta_R & \sin\beta_R & 0 \\ -\sin\beta_R & \cos\beta_R & 0 \\ 0 & 0 & 1 \end{bmatrix}, \quad \mathbf{R}_2 = \begin{bmatrix} 1 & 0 & 0 \\ 0 & \cos\delta_R & -\sin\delta_R \\ 0 & \sin\delta_R & \cos\delta_R \end{bmatrix}, \tag{3}$$

$$\mathbf{R}_3 = \begin{bmatrix} \cos\theta_R & 0 & -\sin\theta_R \\ 0 & 1 & 0 \\ \sin\theta_R & 0 & \cos\theta_R \end{bmatrix}. \tag{4}$$

Since the sweep angle is set to $\beta_R = \beta_L \equiv 0$, we obtain the following rotation matrix which connects the right-wing root frame to the body frame:

$$\boldsymbol{T}_{BR}(\delta_R, \theta_R) = \begin{bmatrix} 1 & 0 & 0 \\ 0 & \cos\delta_R & \sin\delta_R \\ 0 & -\sin\delta_R & \cos\delta_R \end{bmatrix} \times \begin{bmatrix} \cos\theta_R & 0 & \sin\theta_R \\ 0 & 1 & 0 \\ -\sin\theta_R & 0 & \cos\theta_R \end{bmatrix}. \tag{5}$$

A similar matrix $\boldsymbol{T}_{BL}(\delta_L, \theta_L)$ can be derived for the left wing.

3.2. Equations of motion

In the following equations, given a vector $\mathbf{p} = [p_1, p_2, p_3]$, define

$$\mathbf{S}(\mathbf{p}) = \begin{bmatrix} 0 & -p_3 & p_2 \\ p_3 & 0 & -p_1 \\ -p_2 & p_1 & 0 \end{bmatrix}. \tag{6}$$

The equations of translational motion are derived first. Let $\mathbf{r}_{cg}$ denote the position vector of the centre of gravity (CG) of the aircraft, while $\mathbf{r}_{cg,R}$ and $\mathbf{r}_{cg,L}$ denote the position vectors of the CG of the right and left wings in the local wing frame, respectively. Then, the total translational momentum is given by

$$\mathbf{p} = m(\mathbf{u}_B + \mathbf{S}(\boldsymbol{\omega}_B)\mathbf{r}_{cg}) + m_w(\mathbf{S}(\boldsymbol{\omega}_R)\boldsymbol{T}_{BR}\mathbf{r}_{cg,R} + \mathbf{S}(\boldsymbol{\omega}_L)\boldsymbol{T}_{BL}\mathbf{r}_{cg,L}). \tag{7}$$

Using Newton's second law, we obtain

$$\mathbf{F} = m(\dot{\mathbf{u}}_B + \mathbf{S}(\boldsymbol{\omega}_B)\mathbf{u}_B + \mathbf{S}(\dot{\boldsymbol{\omega}}_B)\mathbf{r}_{cg} + \mathbf{S}(\boldsymbol{\omega}_B)\dot{\mathbf{r}}_{cg} + (\mathbf{S}^2(\boldsymbol{\omega}_B)\mathbf{r}_{cg}) + m_w\mathbf{S}(\dot{\boldsymbol{\omega}}_R)\boldsymbol{T}_{BR}\mathbf{r}_{cg,R} + m_w\mathbf{S}^2(\boldsymbol{\omega}_R)\boldsymbol{T}_{BR}\mathbf{r}_{cg,R} + m_w\mathbf{S}(\dot{\boldsymbol{\omega}}_L)\boldsymbol{T}_{BL}\mathbf{r}_{cg,L} + m_w\mathbf{S}^2(\boldsymbol{\omega}_L)\boldsymbol{T}_{BL}\mathbf{r}_{cg,L}, \tag{8}$$

and the CG variation is given by

$$\dot{\mathbf{r}}_{cg} = \frac{m_w}{m}(\mathbf{S}(\boldsymbol{\omega}_R)\boldsymbol{T}_{BR}\mathbf{r}_{cg,R} + \mathbf{S}(\boldsymbol{\omega}_L)\boldsymbol{T}_{BL}\mathbf{r}_{cg,L}). \tag{9}$$

This CG variation could play an important role in cases where the wing weight is substantial and where the CG position is used as a control variable, as in [28].

The total angular momentum is given by

$$\mathbf{h} = m\mathbf{S}(\mathbf{r}_{cg})\mathbf{u}_B + \mathbf{J}\boldsymbol{\omega}_B + \mathbf{J}_R\boldsymbol{\omega}_R + \mathbf{J}_L\boldsymbol{\omega}_L, \quad \mathbf{J}_R = \boldsymbol{T}_{BT}^{\top}\mathbf{J}_{R,R}\boldsymbol{T}_{BT}, \quad \mathbf{J}_L = \boldsymbol{T}_{BL}^{\top}\mathbf{J}_{L,L}\boldsymbol{T}_{BL}. \tag{10}$$

Therefore, the dynamical equations are given by

$$\mathbf{M} = m\mathbf{S}(\dot{\mathbf{r}}_{cg})\mathbf{u}_B + m\mathbf{S}(\mathbf{r}_{cg})\dot{\mathbf{u}}_B + m\mathbf{S}(\boldsymbol{\omega}_B)\mathbf{S}(\mathbf{r}_{cg})\mathbf{u}_B + \mathbf{J}\dot{\boldsymbol{\omega}}_B + \dot{\mathbf{J}}\boldsymbol{\omega}_B + \mathbf{S}(\boldsymbol{\omega}_B)\mathbf{J}\boldsymbol{\omega}_B + \mathbf{J}_R\dot{\boldsymbol{\omega}}_R + \dot{\mathbf{J}}_R\boldsymbol{\omega}_R + \mathbf{S}(\boldsymbol{\omega}_B)\mathbf{J}_R\boldsymbol{\omega}_R + \mathbf{J}_L\dot{\boldsymbol{\omega}}_L + \dot{\mathbf{J}}_L\boldsymbol{\omega}_L + \mathbf{S}(\boldsymbol{\omega}_B)\mathbf{J}_L\boldsymbol{\omega}_L, \tag{11}$$

where

$$\dot{\mathbf{J}}_R = \boldsymbol{T}_{BR}^{\top}(\mathbf{J}_{R,R}\mathbf{S}(\boldsymbol{\omega}_R) - \mathbf{S}(\boldsymbol{\omega}_R)\mathbf{J}_{R,R})\boldsymbol{T}_{BR}, \quad \dot{\mathbf{J}}_L = \boldsymbol{T}_{BL}^{\top}(\mathbf{J}_{L,L}\mathbf{S}(\boldsymbol{\omega}_L) - \mathbf{S}(\boldsymbol{\omega}_L)\mathbf{J}_{L,L})\boldsymbol{T}_{BL}, \quad \dot{\mathbf{J}} = \dot{\mathbf{J}}_R + \dot{\mathbf{J}}_L, \tag{12}$$

and

$$\mathbf{M} = \mathbf{M}_{\text{aero}} + \mathbf{S}(\mathbf{r}_{cg})m\begin{bmatrix} -g\sin\theta \\ g\cos\theta\sin\phi \\ g\cos\theta\cos\phi \end{bmatrix}. \tag{13}$$

In the above equations, $\mathbf{J}_{R,R}$ and $\mathbf{J}_{L,L}$ denote the moments of inertia of the right and left wings, respectively, in their respective local coordinate frames based at the wing root.

For the numerical analysis, the aerodynamic forces and moments are calculated using strip theory. As a method, strip theory is used for aircraft aeroelastic simulations [29] and routinely for blade element theory in the rotorcraft field [30]. Strip theory approaches have also been applied to wings in a trailing vortex flow and aircraft spin prediction (see [31–34] and others cited therein). It seems that only recently has the general strip theory approach been applied in realtime simulation for fixed-wing force and moment calculations [35–39].

In strip theory, the wing is divided into chordwise segments. The local velocity components on each segment are computed to obtain the local angle of attack and sideslip. The lift and drag on each segment are calculated using the local angle of attack and sideslip. The lift and drag forces are summed over the entire wing to yield the net aerodynamic force. The moment due to the force on each segment is computed about the reference point, and these moments are summed over the entire wing to obtain the net aerodynamic moment. Although the aerodynamic contributions of the fuselage and the propulsion mechanism have been ignored here, the results presented in this paper can be readily extended when these aerodynamic contributions are taken into account.

Without any loss of generality, consider the right wing of an aircraft, with (semi) span $b/2$ and chord $c(y)$, where y denotes the spanwise location. Let $\mathbf{V}_{cg} = [u\ v\ w]^{\top}$ denote the body axis wind velocity of the aircraft. Let $[p\ q\ r]$ denote the body axis angular velocity of the fuselage.

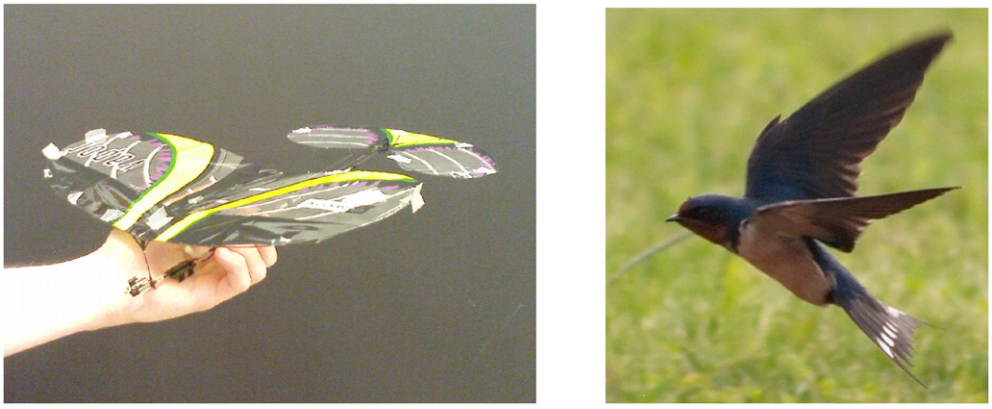

(*a*) (*b*)

Figure 3. The figure on the left shows ParkZone®Vapor, the aircraft model used for the analysis in this paper. The size of the Vapor is similar to that of small birds such as the barn swallow shown on the right. (*a*) ParkZone®Vapor: the aircraft model considered in the paper (without the vertical tail). (*b*) A barn swallow (*Hirundo rustica*) in flight, taken in Milwaukee, WI (source: wikimedia.org, author: 'Dori', licence: CC BY-SA 3.0, available at: http://commons.wikimedia.org/wiki/File:Barn_swallow_6909.jpg).

The angular velocity perceived at a spanwise strip at a distance y along the span is given by

$$\Omega_R = \begin{bmatrix} p \\ q \\ r \end{bmatrix} + \begin{bmatrix} 0 \\ 0 \\ \dot{\beta}_R \end{bmatrix} + \mathbf{R}_1^{\mathrm{T}} \begin{bmatrix} -\dot{\delta}_R \\ 0 \\ 0 \end{bmatrix} + \mathbf{R}_1^{\mathrm{T}} \mathbf{R}_2^{\mathrm{T}} \begin{bmatrix} 0 \\ \dot{\theta}_R \\ 0 \end{bmatrix} \tag{14}$$

and the local velocity at that strip on the right wing is

$$\mathbf{V}(y) = \mathbf{V}_{cg} + \mathbf{S}(\Omega_R)\mathbf{r}_{ac}, \tag{15}$$

where $\mathbf{r}_{ac}$ is the position vector of the aerodynamic centre of the station given by

$$\mathbf{r}_{ac} = \mathbf{R}_1^{\mathrm{T}} \mathbf{R}_2^{\mathrm{T}} \mathbf{R}_3^{\mathrm{T}} \begin{bmatrix} x_{ac} \\ y \\ 0 \end{bmatrix}, \tag{16}$$

where x_{ac} is the chordwise location of the aerodynamic centre with respect to the mid-chord. It is assumed to be $c/4$. The local aerodynamic force at the station is given by the vector sum of the lift and the drag, with components written in the body frame:

$$\mathrm{d}\mathbf{F} = 0.5\rho \|\mathbf{V}(y)\|^2 c(y)(C_L \mathbf{l}/\|\mathbf{l}\| + C_D \mathbf{d}/\|\mathbf{d}\|)\,\mathrm{d}y, \tag{17}$$

where

$$\mathbf{l} = -\mathbf{S}(\mathbf{V}(y))\mathbf{R}_1^{\mathrm{T}} \mathbf{R}_2^{\mathrm{T}} \mathbf{R}_3^{\mathrm{T}} [0\ 1\ 0]^{\top} / \|\mathbf{V}(y)\|, \tag{18}$$

$$\mathbf{d} = -\mathbf{V}(y)/\|\mathbf{V}(y)\|. \tag{19}$$

Section 4 discusses the C_L and C_D expressions in detail. The local aerodynamic moment at the station is given by

$$\mathrm{d}\mathbf{M} = \mathbf{S}(\mathbf{r})\mathrm{d}\mathbf{F} + \rho \|\mathbf{V}(y)\|^2 c(y) C_{\mathrm{m_{ac}}} \mathbf{R}_1^{\mathrm{T}} \mathbf{R}_2^{\mathrm{T}} \mathbf{R}_3^{\mathrm{T}} [0\ 1\ 0]^{\top}\,\mathrm{d}y. \tag{20}$$

The total aerodynamic force and moment are obtained by integrating the above expressions, performed in practice by using strip theory, as explained earlier. The forces can be projected onto the wind axes and these, together with the moments, can be substituted into equations (8) and (13). The term $C_{\mathrm{m_{ac}}}$, as explained in section 5, plays an important role in determining the effectiveness of the wing dihedral for yaw control.

The kinematic equations relate the angular velocity of the aircraft to the rates of change of the Euler angles:

$$\begin{aligned} \dot{\phi} &= p + q \sin\phi \tan\theta + r \cos\phi \tan\theta \\ \dot{\theta} &= q \cos\phi - r \sin\phi \\ \dot{\psi} &= (q \sin\phi + r \cos\phi)/\cos\theta. \end{aligned} \tag{21}$$

The equations which relate the position of the aircraft to its translational velocity are essentially decoupled from the flight dynamics, and are given by

$$\begin{aligned} \dot{X} &= V \cos\gamma \cos\chi \\ \dot{Y} &= V \cos\gamma \sin\chi \\ \dot{Z} &= -V \sin\gamma. \end{aligned} \tag{22}$$

The flight path angle (γ) and the wind axis heading angle (χ) in equation (22) are defined as follows:

$$\begin{aligned} \sin\gamma &= \cos\alpha \cos\beta \sin\theta - \sin\beta \sin\phi \cos\theta \\ &\quad - \sin\alpha \cos\beta \cos\phi \cos\theta \\ \sin\chi \cos\gamma &= \cos\alpha \cos\beta \cos\theta \sin\psi \\ &\quad + \sin\beta(\sin\phi \sin\theta \sin\psi + \cos\phi \cos\psi) \\ &\quad + \sin\alpha \cos\beta(\cos\phi \sin\theta \sin\psi - \sin\phi \cos\psi). \end{aligned} \tag{23}$$

The turn rate is given by $\omega = \dot{\psi}$. If $\dot{\theta} = \dot{\phi} = 0$, it follows that

$$\omega = \dot{\psi} = \mathrm{sign}(\dot{\psi})\sqrt{p^2 + q^2 + r^2}. \tag{24}$$

The above expression is used to compute the equilibrium turn rate during trim analysis.

4. Aircraft model and aerodynamics

The aircraft model considered in this paper is derived from the Vapor shown in figure 3(*a*)[1] by removing the vertical tail and the propeller. To simplify the analysis, the aerodynamic contributions of the fuselage and the propulsive mechanism are neglected with the understanding that they can be readily added within the conceptual framework of this paper. The

[1] http://www.parkzone.com/Products/Default.aspx?ProdID=PKZ3380.

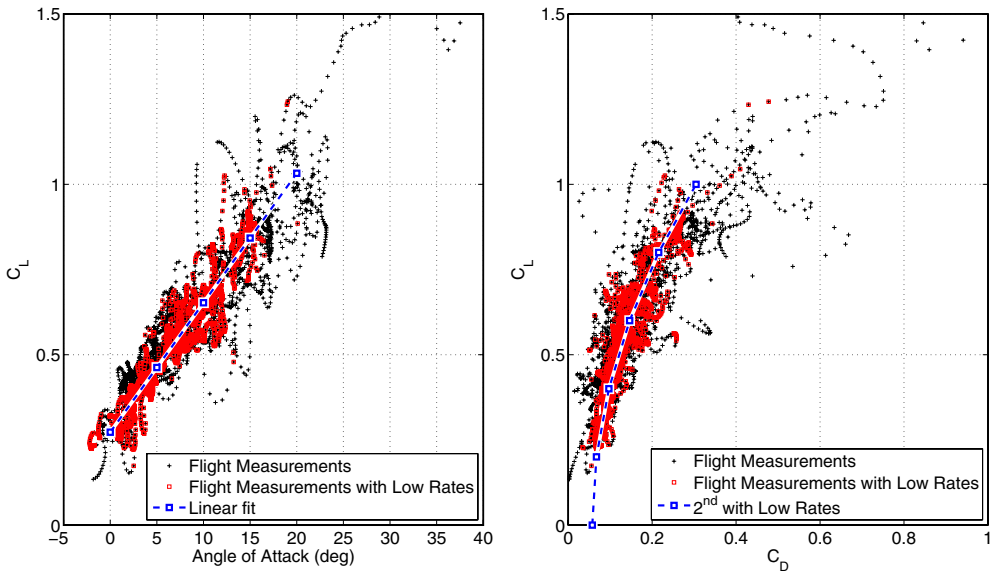

Figure 4. Experimentally obtained aerodynamic data [25].

wings have an elliptic planform. As explained in the next section, the problem of adverse yaw in the absence of a vertical tail may be ameliorated by placing the CG behind the wing AC. The dimensions of the Vapor are similar to those of small birds such as the barn swallow shown in figure 3(*b*)[2].

The lift and drag coefficients of the wing and tail airfoils, adapted from values determined experimentally [25] for the Vapor itself (shown in figure 3(*a*)) at a Reynolds number of 20 000, are given by

$$C_L = 0.28295 + 2.00417\alpha, \qquad C_D = 0.0346 + 0.3438C_L^2, \tag{25}$$

where α is measured in radians. Using thin airfoil theory [40], it was determined that $C_{m_{ac}} = -0.1311$. The actual experimental plot has been shown in figure 4. The C_L and C_D expressions in equation (25) are obtained by averaging *only* over the red points in figure 4. The rest of the points in figure 4 (marked in black) represent data collected at high values of pitch rate and $\dot{\alpha}$, and are not relevant to the discussion in this paper. During the experiments, for $\alpha > 25$ deg, $\dot{\alpha}$ was seen to be substantial and therefore, the coefficients in equation (25) are reliable only up to $\alpha = 25$ deg.

The aircraft weighs 12 g, including a ballast mass added to the nose of the aircraft for placing the CG around half-wing-chord under nominal conditions, i.e. when the wing dihedral and incidence are both zero. The aircraft is 29.7 cm long from nose to tail, and under nominal conditions, the distance between the AC and the CG is $x_{ac} = 3.6$ cm. The horizontal tail is located 26.1 cm behind the wing root AC. The limiting value of the horizontal tail deflection is assumed to be 30 deg in both directions. The limiting value of the wing dihedral is assumed to be 60 deg on either side, while that of the wing incidence is 15 deg.

[2] http://commons.wikimedia.org/wiki/File:Barn_swallow_6909.jpg.

5. Results on stability and performance

This section describes the main results of the paper. The effectiveness of wing dihedral for yaw control is compared with that of the vertical tail in section 5.1. Sections 5.2 and 5.3 describe a linear analysis of lateral-directional stability and lay the foundation for a formal analysis of the control effectiveness of wing dihedral for yaw control in section 5.4 as well as the bifurcation analysis in sections 5.5 (longitudinal flight) and 5.6 (turning flight).

5.1. Analytical comparison with the vertical tail

Figure 5 illustrates the physics underlying the use of wing dihedral as a control. Increasing the wing dihedral reduces the force acting in the body z-direction, and generates a side force. The reduced z-force affects the aircraft flight path angle and angle of attack, and hence the flight speed. On the other hand, the side force can be used for providing the centripetal force for turning and as a source of the yawing moment. In particular, if the CG is located behind the line of action of the side force, then a positive side force produces a positive yawing moment and vice versa (see figure 2 for the sign conventions). It follows that a positive rolling moment (wherein the lift on the left wing is higher than the right wing) is accompanied by a positive yawing moment if the wings have a positive dihedral deflection. Consequently, the adverse yaw produced due to rolling is reduced.

Figure 5 qualitatively suggests candidate dihedral deflections of the two wings in order to perform a turn. For example, to turn right, the left wing could be deflected upwards and the right wing downwards about a symmetric setting. While such a setting would provide the required side force, it could lead to an adverse yaw moment arising from the z-axis projections of the pitching moments about the AC of the two wings. The adverse yaw moment, which would be produced by wings with substantial positive camber, could potentially inhibit the turn.

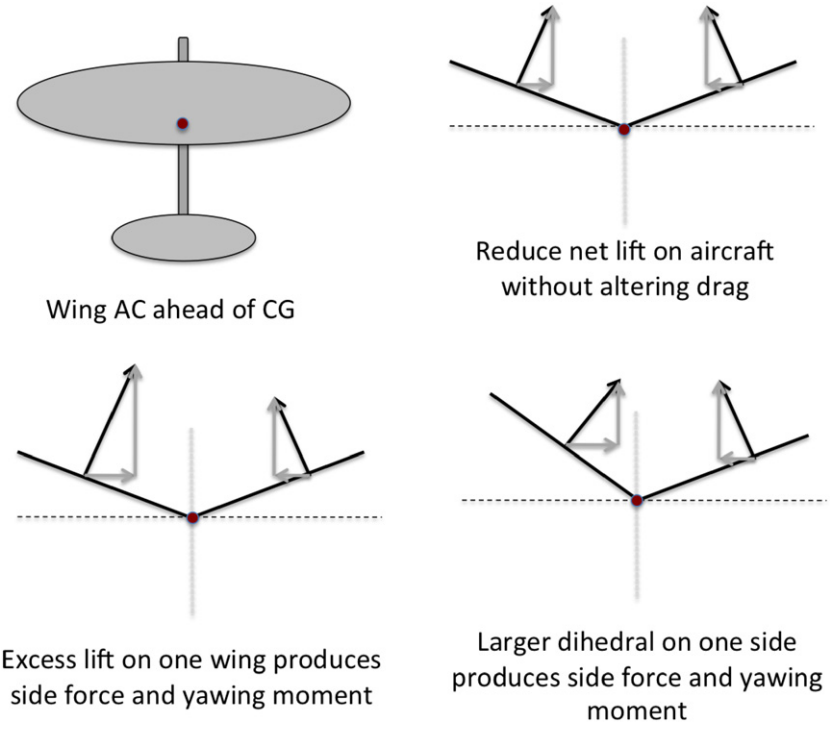

Figure 5. Illustration of the physics underlying the use of dihedral as a control. The dark conspicuous dot in the figures is the aircraft CG.

In order to appreciate the utility and the limitations of using differential dihedral as the yaw control mechanism, the yawing moment produced by the differential dihedral should be compared with that of a conventional vertical tail. In order to provide a basis for a fair comparison, the deflection of the tail and the differential dihedral are kept identical. Consider a rectangular vertical tail with a span b_t, chord c_t, area $S_t = b_t c_t$, and located at a distance l_t behind the CG. The wing has a semi-span $b/2$ and chord c. Let S_w denote the area of each wing, and let l_w denote the x-component of the moment arm of the side force with respect to the CG, where $l_w > 0$ is the wing AC that is ahead of the CG. The yawing moment produced by the vertical tail is calculated by assuming that the dihedral deflection of both wings is zero. In order to simplify the analysis, let α_w denote the effective angle of attack of the wing, i.e. $C_L(\alpha) = C_{L_\alpha}\alpha_w$. Generally, $\alpha_w \neq \alpha$ for cambered wings.

Assuming a linear relation between the lift and the angle of attack, the yawing moment generated by the tail for a deflection $\beta_t > 0$ is equal to $N_t = q_\infty S_t l_t C_{L_\alpha}\beta_t$, where q_∞ is the dynamic pressure. The moment generated by a dihedral deflection, δ, of the left wing, while that of the right wing is zero, is given by

$$N_w = q_\infty S_w (l_w C_{L_\alpha}\alpha_w + c C_{\mathrm{m_{ac}}})\delta. \tag{26}$$

If $\beta_t = \delta$, then the dihedral effectiveness ratio, $\zeta = N_w/N_t$, is given by

$$\zeta = \frac{S_w l_w}{S_t l_t}\alpha_w + \frac{S_w c}{S_t l_t}\frac{C_{\mathrm{m_{ac}}}}{C_{L_\alpha}}. \tag{27}$$

Clearly, the dihedral is more effective for yaw control at high angles of attack. Equation (27) also suggests that the dihedral is better than the vertical tail when l_t is small. The ability to change wing dihedral is built into the birds in the form of their ability to flap their wings for propulsion. Hence, no additional mechanisms are needed for yaw control. Ornithopters, too, can benefit from differential dihedral-based yaw control in a similar manner.

Remark. For positively cambered wings, $C_{\mathrm{m_{ac}}} < 0$. Hence the second term on the right-hand side of (27) is negative. This term not only reduces ζ, but could also render it negative. In the latter case, the left wing could be deflected downwards, or the right wing could be deflected instead of the left wing. Alternately, if the wing camber can be controlled independently, the camber could be chosen to make $C_{\mathrm{m_{ac}}}$ small enough so that the dihedral effectiveness ratio, ζ, is positive. There is no evidence in the literature to suggest whether birds perform cambering for the aforementioned purpose. It is known that cambering can be used for other purposes such as high lift generation, delaying stall and flutter prevention [41]. From a design perspective, the argument stated here suggests that the wing airfoil should be chosen with as small a camber as possible when the wing dihedral is to be employed for yaw control.

The idea of using wing dihedral for control is particularly useful when the wings are flexible, because flexible wings bend and twist spontaneously under aerodynamic loading. The dihedral angle at a given point on the wing is equal to the sum of the slope of the bending displacement and the wing slope at the root. Since bending and twisting are coupled, wing twist that can be used bring about a passive proverse change in the wing dihedral [42].

A brief theoretical analysis is in order before a computational analysis is performed. The objectives of the

Table 2. Stability derivatives for a tailless aircraft with an articulated wing.

Derivative	Symmetric flight ($\delta_L = \delta_R = \delta$)	Turning flight ($\delta_L \approx -\delta_R$)	Stability condition
L_β	Stable	Stable when $\delta_L + \delta_R > 0$ (see section 5.4)	$L_\beta < 0$
L_p	Stable	Stable	$L_p < 0$
N_β	Unstable	Unstable	$N_\beta > 0$
N_r	Stable (drag reduces stability)	Unstable, but stable when $\text{sign}(p) \neq \text{sign}(\delta_L - \delta_R)$ (section 5.4)	$N_r < 0$

next three subsections are to (a) derive analytical expressions for estimating the contribution from the wings to force and moment derivatives, (b) identify the lateral modes using the standard fourth order model, and (c) estimate the sign of the control effectiveness of asymmetric dihedral for turning.

5.2. Analytical approximations to lateral-directional stability

The lift and drag forces produced by the wing as well as their moments about the origin of the body frame can be resolved along the body axes. In particular, summing the body axis components of the net moment due to lift and drag yields the net rolling, pitching and yawing moments. The stability of aircraft depends primarily on the three aerodynamic moments and their derivatives with respect to the aircraft angular velocity, angle of attack and sideslip.

Let α and β denote the angle of attack and sideslip, i.e. $w = u\tan\alpha$ and $v = V_\infty \sin\beta$ where u, v and w are components of the aircraft velocity along the aircraft body axes. Consider the aerodynamic centre of a wing cross section, with coordinates $[x, y, 0]$ in the wing frame. Ignoring the angle of incidence of the wing with respect to the fuselage, the local wind velocity at the aerodynamic centre in question is given by

$$\mathbf{v}_{\text{loc}} = \begin{bmatrix} u - y(q\sin\delta + r\cos\delta) \\ v\cos\delta - w\sin\delta + x(q\sin\delta + w\cos\delta) \\ v\sin\delta + w\cos\delta + py - x(q\cos\delta - r\sin\delta) \end{bmatrix}. \quad (28)$$

If q is ignored to restrict the analysis to lateral-directional motion, it follows that the local angle of attack is given by

$$\alpha_{\text{loc}} \approx \frac{\beta\sin\delta + \alpha\cos\delta + \frac{py + rx\sin\delta}{u}}{1 - \frac{ry}{u}\cos\delta}, \quad (29)$$

which can be simplified further using binomial expansion of the denominator to yield

$$\alpha_{\text{loc}} \approx \beta\sin\delta + \alpha\cos\delta + \frac{py + rx\sin\delta}{u} + \frac{ry}{u}\alpha\cos\delta + \frac{pry^2\cos\delta}{u^2}. \quad (30)$$

At low to moderate angles of attack, the net force along the body z-axis is approximated by $Z \propto \alpha_{\text{loc}}$. Furthermore, the rolling and yawing moments can be approximated by

$$L \propto Z_L - Z_R, \quad N \propto (Z_L\sin\delta_L - Z_R\sin\delta_R). \quad (31)$$

The lateral-directional derivatives can be approximated as follows:

$$L_\beta \propto -u^2(\delta_L + \delta_R), \quad L_p \propto -ub, \quad L_r \propto -ub\alpha \quad (32)$$

$$N_\beta \propto -u^2(\delta_L^2 + \delta_R^2), \quad N_p \propto -ub(\delta_L + \delta_R) + r\frac{b^2}{2}(\delta_L - \delta_R),$$
$$N_r \propto -ub\alpha(\delta_L + \delta_R) + \left(\frac{pb^2}{2}\right)(\delta_L - \delta_R). \quad (33)$$

Useful information about aircraft stability can be gleaned from equations (32) and (33), which has been tabulated in table 2.

Based on the results in table 2, it is clear that the aircraft would be expected to be unstable in most flight regimes. At least two stability derivatives suggest the possibility of stability in some select turn regimes. However, in rapid turn regimes, the flight dynamics are far too strongly coupled to draw reliable conclusions from this linear, decoupled analysis. Furthermore, because the stability derivatives depend strongly on the wing dihedral angle, which is in turn a function of the aircraft manoeuvre, it follows that stability is tied very closely to the nature of the manoeuvre being executed. The observation is peculiar to aircraft with articulated wings. In conventional aircraft with fixed wings, although stability derivatives depend on aircraft states, they are essentially independent of the control surface deflection.

5.3. Lateral-directional stability

Figure 6(*a*) shows the root locus plot for a sample flight speed of $2\,\text{m}\,\text{s}^{-1}$. The highly stable roll mode is not shown here. The root locus plot is obtained by varying the angle of attack for four candidate symmetric dihedral deflections: 6 deg (black), 17 deg (blue), 28 deg (red), and 40 deg (magenta). The root locus plot helps to verify some of the observations in section 5.2. The unstable stability derivatives observed in table 2 manifest in the form of an unstable Dutch roll mode. Figure 6(*b*) plots the real part of the rightmost eigenvalue, which measures the stability margin of the dynamics. The Dutch roll mode is seen to stabilize around $\alpha = 7\,\text{deg}$ for three candidate dihedral deflections, except for $\delta = 6\,\text{deg}$. In the latter case, the complex conjugate Dutch roll eigenvalues merge on the real axis, and one eigenvalue moves to the right with increasing α worsening the instability. Clearly, the Dutch roll mode shows a qualitatively different, more desirable behaviour for large dihedral deflections.

Figure 6(*c*) is a plot of the real part of the rightmost eigenvalue for $V = 3\,\text{m}\,\text{s}^{-1}$. The effect of flight speed is summed up in the observation that the Dutch roll mode stabilizes at a much higher angle of attack for the three larger symmetric dihedral deflections. A strong dependence of stability characteristics on the flight speed is another

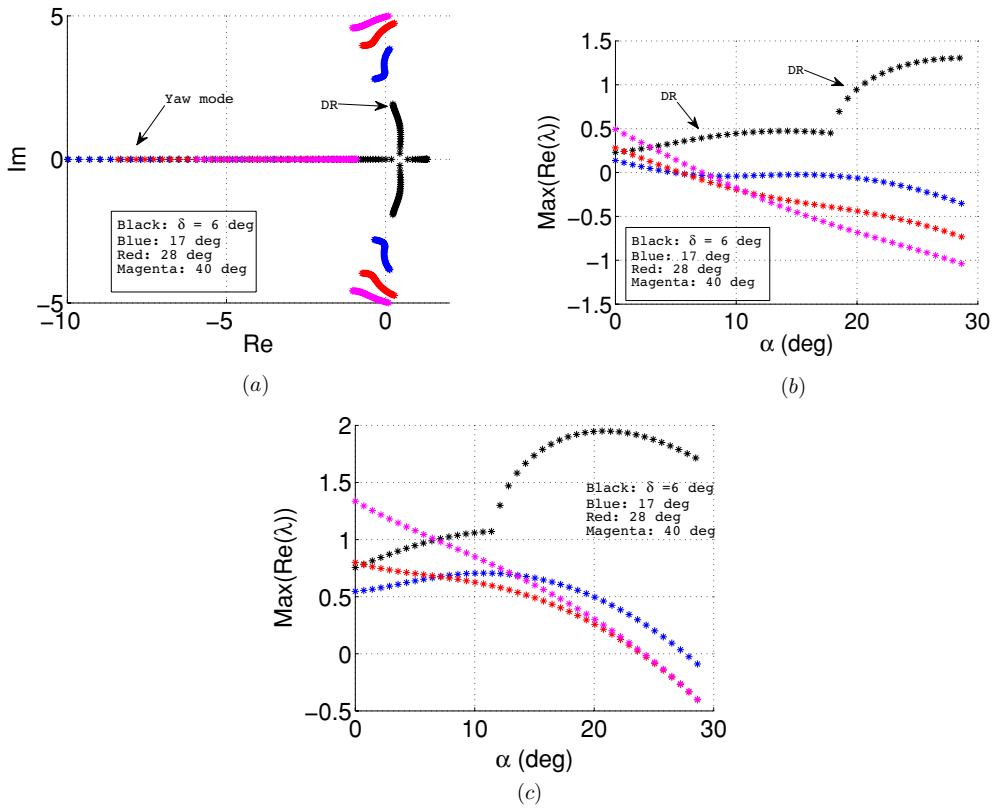

Figure 6. Root locus plot showing lateral-directional eigenvalues as functions of the angle of attack for candidate symmetric wing dihedral deflections. The roll mode is not shown in the root locus plot. The real part of the rightmost eigenvalue is a measure of the stability margin when the system is stable. (*a*) Root locus for $V = 2\,\mathrm{m\,s^{-1}}$. (*b*) Real part of the rightmost eigenvalue for $V = 2\,\mathrm{m\,s^{-1}}$. (*c*) Real part of the rightmost eigenvalue for $V = 3\,\mathrm{m\,s^{-1}}$.

feature of the low speed flight of MAVs. In contrast, the stability of faster, heavier fixed wing aircraft depends primarily on the angle of attack in pre-stall, incompressible flow regimes.

5.4. Control effectiveness for turning

The wing dihedral angles may be changed asymmetrically for executing turns as explained earlier in section 5.1. The challenge would be to design control laws for controlling the yaw rate and the roll rate for which it is necessary to determine the control effectiveness of the wing dihedral. Specifically, the control effectiveness is measured in terms of incremental rolling and yawing moments generated by an incremental change in the wing dihedral angles.

A logical scheme for designing a yaw control law would be to use δ_L–δ_R to control the turning rate. This is akin to controlling the aircraft bank angle as a function of the commanded turn rate. From equation (30), it is clear that the incremental change in α_{loc} is a nonlinear function of δ_L–δ_R and it depends on angular velocity of the aircraft as well. Therefore, it is perfectly possible that the sign of the control effectiveness need not be uniform across the flight regime. The yaw control effectiveness is particularly interesting because of its strong sensitivity to the dihedral angles.

Figures 7(*a*)–(*c*) plot the sign of the control effectiveness, i.e. $\mathrm{sign}\left(\frac{\Delta N}{\Delta(\delta_L-\delta_R)}\right)$, on a $p-r$ grid for angles of attack of 5.73 deg (0.1 rad), 8.595 deg (0.15 rad) and 11.46 deg (0.2 rad). Similar plots for other angles of attack have been omitted for brevity. The plots clearly show that the sign of the control effectiveness is negative at low angles of attack. The sign depends strongly on the angular rates between angles of attack of 6 deg and 12 deg, and it is positive uniformly thereafter. The sign of the control effectiveness is usually assumed to be known *a priori* while designing control laws. The challenge involved in designing a sound turning flight controller is captured in figure 7.

5.5. Stability and longitudinal performance of symmetric configurations

This subsection illustrates the effect of dihedral on the performance and stability when the aircraft configuration is symmetric, i.e. $\delta_R = \delta_L = \delta$. The wing incidence and sweep are both set to zero.

The following notation has been adopted for the bifurcation diagrams: an asterisk '$*$' denotes an unstable equilibrium where eigenvalues with positive real parts are all real. Conversely, an empty circle '$\circ$' denotes an unstable equilibrium where the eigenvalues with positive real parts arise in complex conjugate pairs. A filled circle ($\cdot$), occasionally coloured for clarity, denotes an unstable equilibrium where the eigenvalues with positive real parts consist of real as well as complex conjugate eigenvalues. Bifurcation points denote a qualitative change in the stability of the aircraft. Interestingly enough, no stable trims were observed for the aircraft.

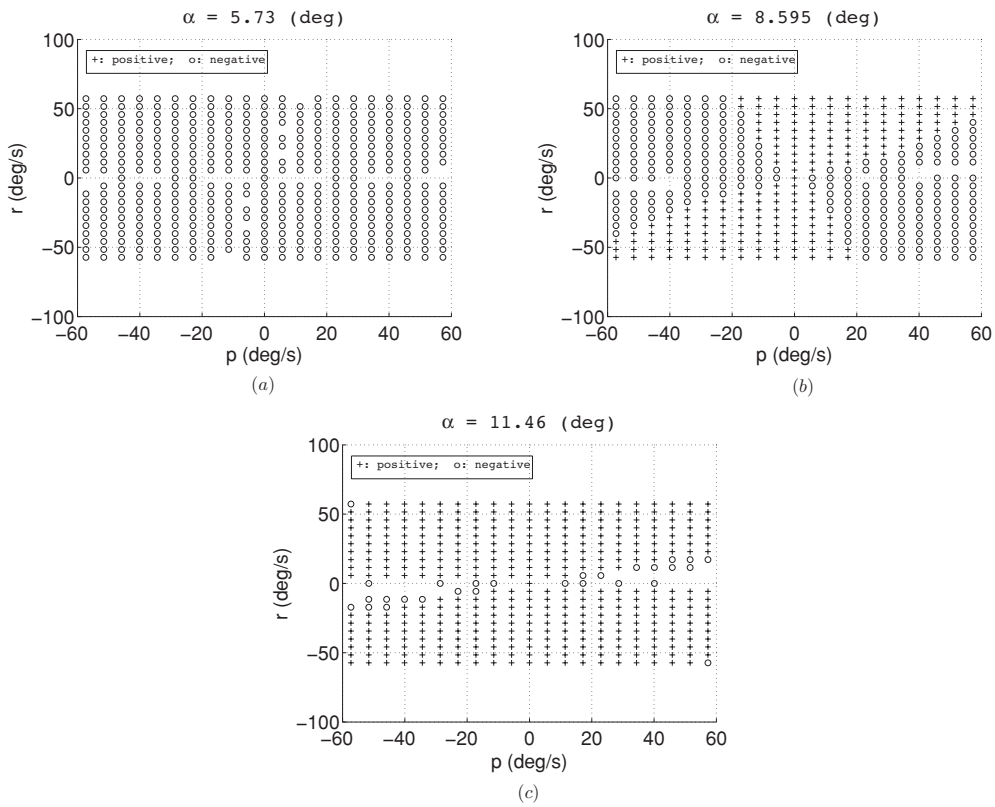

Figure 7. Plots showing the sign of the control effectiveness, sign($\frac{\Delta N}{\Delta(\delta_L - \delta_R)}$), as a function of the angle of attack, roll rate and yaw rate. (*a*) Control effectiveness at $\alpha = 5.73$ deg. (*b*) Control effectiveness at $\alpha = 8.595$ deg. (*c*) Control effectiveness at $\alpha = 11.46$ deg.

A key observation is that the use of symmetric dihedral offers the possibility of independently controlling two of the three longitudinal performance metrics, namely the flight speed, angle of attack and the flight path angle. This cannot be achieved in fixed wing aircraft without variable thrust or variable dihedral. The Euler pitch angle would be an enterprising addition to the list of variables, with applications to airborne visual tracking of other airborne vehicles or ground-based objects.

Figures 8(*a*) and (*b*) show the flight path angle and the angle of attack, respectively, as functions of the wing dihedral angle when the flight speed is held at an arbitrarily chosen value $2.8\,\mathrm{m\,s^{-1}}$. The wing dihedral is varied between -50 and 50 deg, and figure 8(*c*) shows the elevator schedule, as a function of the wing dihedral, required to maintain the aforementioned flight speed.

All the equilibria are laterally unstable. It is worth pointing out that the longitudinal modes are stable. The equilibria in the small patch between $\delta = -33$ deg and $\delta = 0$ are unstable with a pair of complex conjugate values, while for all other equilibria, the positive eigenvalues are real. An aircraft trimmed at any of these equilibria would diverge away from it, and the post-departure behaviour can be determined only after further trim analysis or simulations. The steady states constituting post-departure behaviour would not be routinely flown by the aircraft and, as such, they would represent highly undesirable flight conditions. Hence, no attempt has been made to determine the post-departure steady states as part of the bifurcation analysis.

Figure 9 shows a simulated time history of the aircraft motion. The wing dihedral angles were both set to 10 deg, while the elevator was set to -10 deg. The initial angle of attack was 5 deg, while all the lateral variables (β, p, r, ϕ) were set to zero. The aircraft seems to stabilize for the first 4 s before departing rapidly into a fast spin-like dive. Since the initial value of all lateral states was zero, and the longitudinal modes are stable, the aircraft tends to stabilize itself in the absence of any lateral inputs or disturbances. The lateral variables acquire non-zero values from numerical integration errors. The sideslip and the lateral angular rates build up due to the lateral instability, while the pitch rate and angle of attack are affected by the lateral–longitudinal coupling.

Remark. Strictly speaking, the simulation time histories in figure 9 are of limited accuracy because the aerodynamic data are available up to an angle of attack of 25 deg only. However, the aforementioned explanation about aircraft stability is correct because it pertains to the low-α trim states.

5.6. Lateral stability and performance

The wing incidence angles can be set anti-symmetrically on the two wings to generate rolling moment, and differential dihedral can serve as a yaw control mechanism as explained earlier in the paper. The equilibrium turn rate, defined in

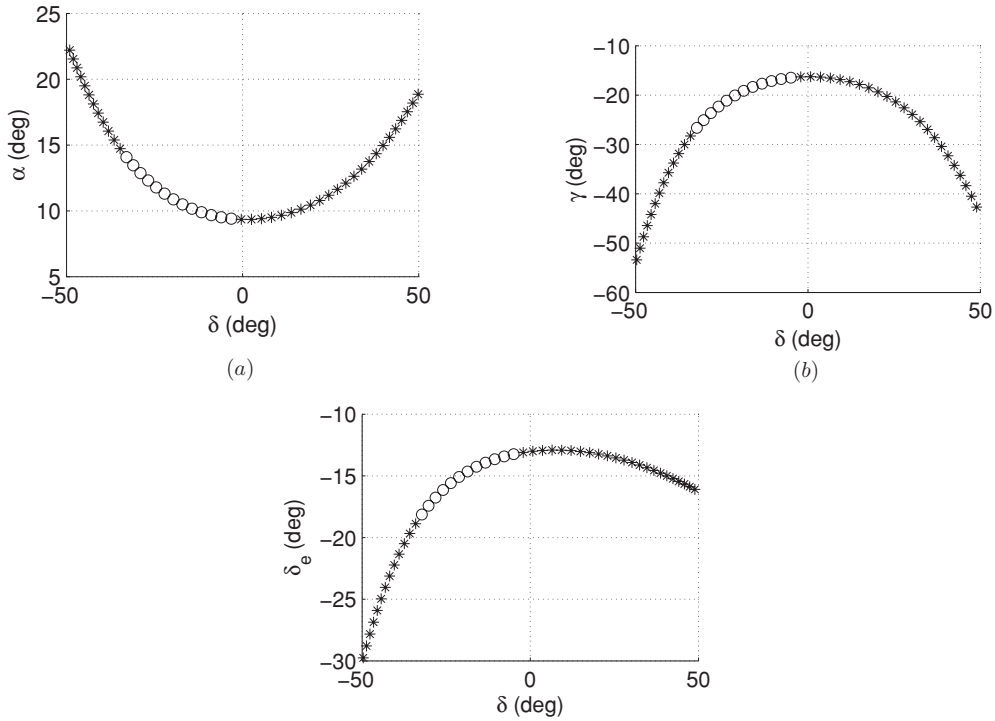

Figure 8. Bifurcation diagrams showing γ and α versus symmetric dihedral (i.e. $\delta_R = \delta_L = \delta$), and the corresponding elevator deflection to hold the speed fixed at $V = 2.8\text{m}\,\text{s}^{-1}$. (a) Angle of attack as a function of dihedral. (*b*) Flight path angle as a function of the dihedral. (*c*) Elevator as a function of the dihedral.

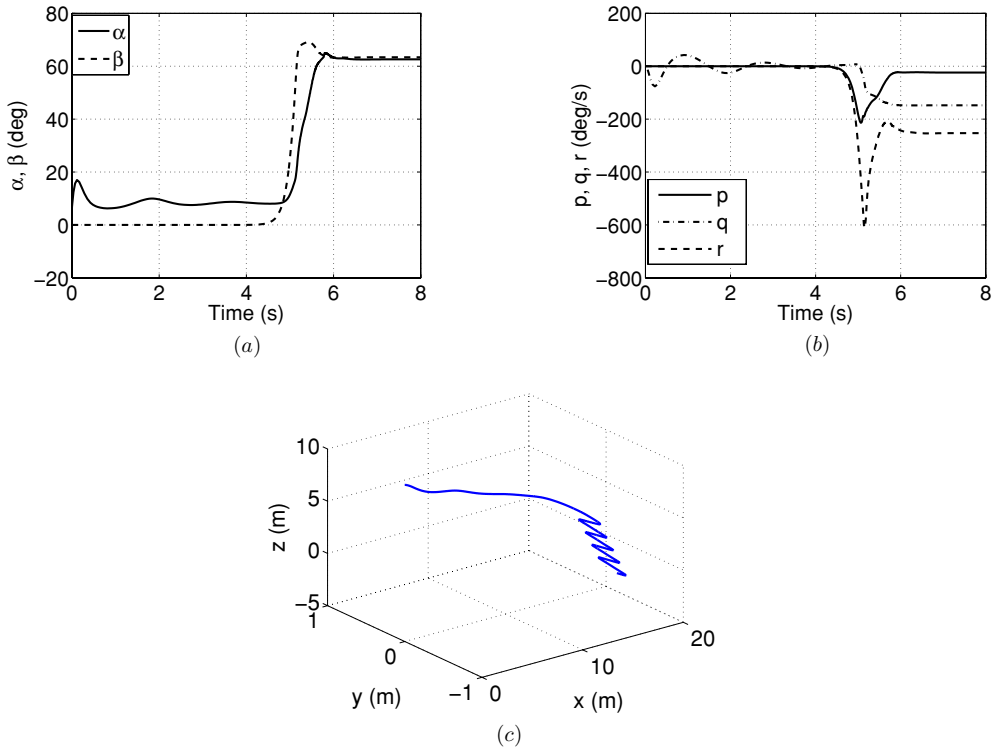

Figure 9. Simulated time history of the aircraft motion with the dihedral angle of both wings fixed at 10 deg. All lateral variables, namely the sidelip, roll rate, yaw rate and the Euler roll angle, were initialized at zero. (a) Angle of attack and sideslip time histories. (*b*) Time histories of the roll, pitch and yaw rates. (*c*) Trajectory in the x, y, z plane.

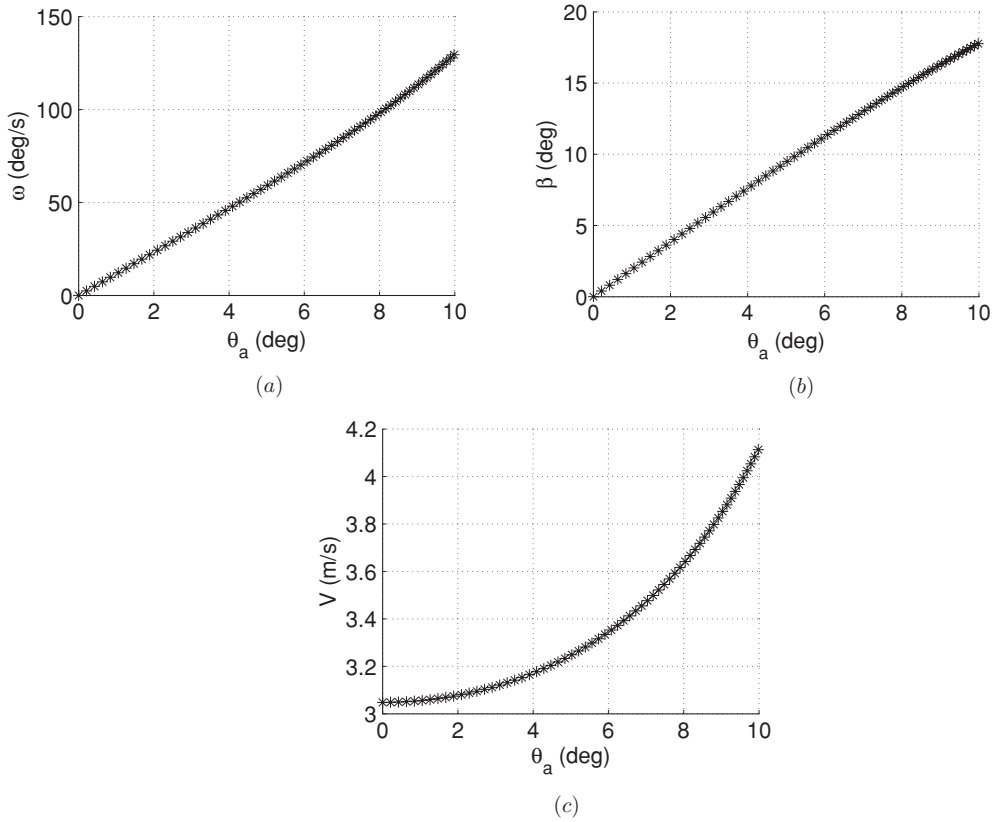

Figure 10. Case 1: turn rate, sideslip and flight speed as functions of the anti-symmetric wing incidence. The wing dihedral angles were fixed at 29 deg. (*a*) Turn rate (ω) as a function of antisymmetric wing incidence (left wing positive). (*b*) Sideslip (β) as a function of antisymmetric wing incidence. (*c*) Flight speed (V) as a function of antisymmetric wing incidence.

Table 3. Four cases considered in this section and their physical significance.

Dihedral angles	Incidence angles	Constraints	Physical significance
Symmetric, non-zero	Anti-symmetric	None	Turn using just the wing incidence
$\delta_R = 0$, δ_L freed	Anti-symmetric	$\beta = 0$	Turn and maintain zero sideslip
$\delta_L \neq \delta_R$ (asymmetric variation)	Zero	$\beta = 0$	Turn using only the wing dihedral and maintain zero sideslip
Asymmetric	Anti-symmetric	$\beta = 0$, V prescribed	Compute achievable turn rate for given speed and maintain zero sideslip

equation 24, is an important agility metric for an aircraft [44]. Bifurcation analysis is used for analysing performance and stability for the four benchmark cases in table 3.

5.6.1. Case 1 (variable θ_L; $\theta_R = -\theta_L$; $\delta_L = \delta_R$ held fixed). Consider the first case where the wing incidence is varied anti-symmetrically. Physically, this case represents a turn without any dedicated yaw control mechanism. Instead, the roll rate generated by the anti-symmetric wing incidence angles, coupled with the dihedral effect modelled in section 5.2, leads to a yawing moment which, in turn, generates the yaw rate. Because there is no dedicated yaw controller, the sideslip is not regulated and grows with increasing turn rate.

Figures 10(*a*)–(*c*) plot the turn rate ω, sideslip angle β and the flight speed V as functions of the incidence angle when $\delta = 29$ deg. It is observed that large values of turn rate are achieved with relatively small values of wing incidence. The sideslip angle and the flight speed increase as the turn rate increases with increasing wing incidence. The sideslip angle eventually builds up to nearly 18 deg, while the flight speed is consistently greater than 3.1 m s^{-1}. All trim solutions are seen to be unstable with a positive real eigenvalue.

Given the subsequent increase in sideslip and flight speed with increasing turn rate when the dihedral angles on the two wings are equal and constant, it is valid to ask whether rapid turns can be performed while maintaining zero sideslip and a prescribed flight speed. An alternate way of restating this question is to ask whether an arbitrary desired turn rate can

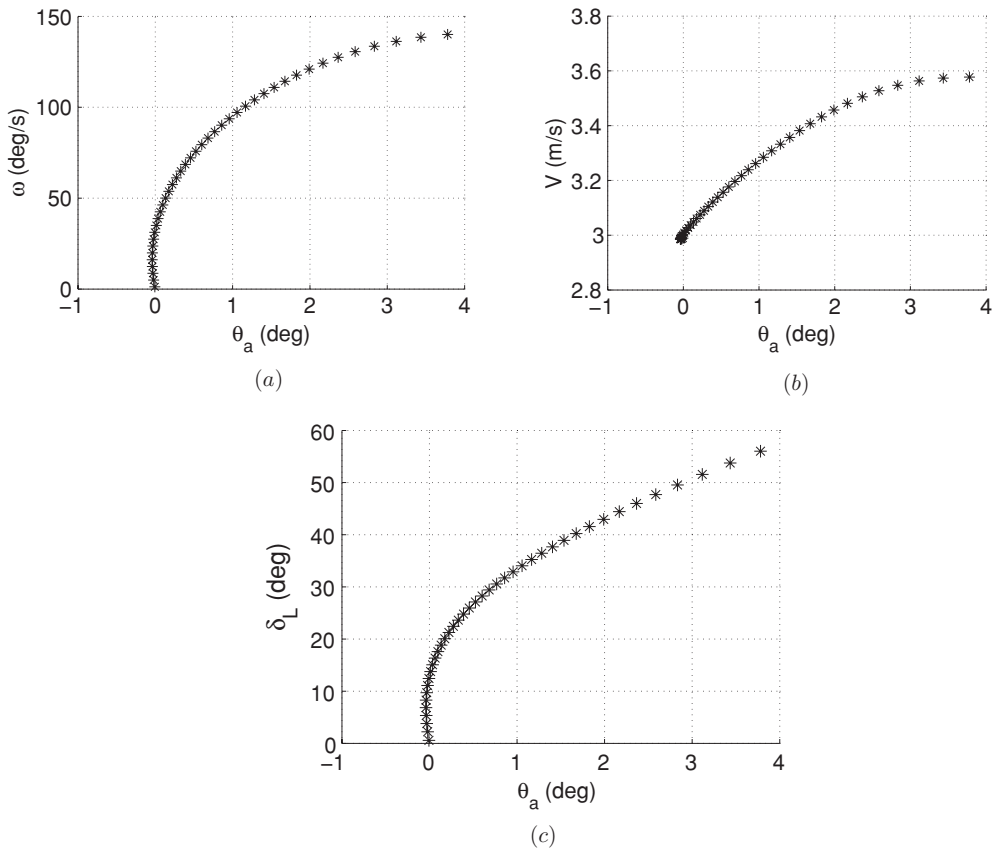

Figure 11. Case 2: coordinated turn trims as a function of anti-symmetric wing incidence. (*a*) Turn rate (ω) as a function of antisymmetric wing incidence with constraint $\beta = 0$. (*b*) Flight speed (V) as a function of antisymmetric wing incidence with constraint $\beta = 0$. (*c*) Wing dihedral δ_L required to maintain $\beta = 0$.

be achieved for a given flight speed and with zero sideslip. In order to accommodate constraint equations corresponding to zero sideslip and constant flight speed, the corresponding control parameters, in this case the dihedral angles of both wings, are 'freed', i.e. treated as de facto state variables. The resulting larger set of equations is then solved to compute the aircraft trim states and control inputs needed to achieve those trims. In order to infer the stability of the trim states, the Jacobian corresponding to the original set of differential equations is isolated, and its eigenvalues are computed.

5.6.2. Case 2 (variable θ_L; $\theta_L = -\theta_R$; δ_L free for $\beta = 0$; $\delta_R = 0$). Consider the second case where the sideslip is required to be zero, while the flight speed is not constrained.

The left wing dihedral is freed to provide the yawing moment necessary to regulate sidelsip to zero, while the right-wing dihedral is held fixed at zero. As an alternative, the right dihedral may be scheduled to maintain some other flight parameter, as illustrated later in the section. Figures 11(*a*)–(*c*) plot the turn rate, the flight speed and the left wing dihedral as functions of the antisymmetric wing incidence. All trim solutions are seen to be unstable. Initially, increasing ω and δ_L are accompanied by a reduction in the wing incidence. Thereafter, the turn rate and the left wing dihedral increase monotonically with the wing incidence. The dihedral angle required to maintain zero sideslip is close to its saturation value of 60 deg when the wing incidence is 4 deg and the corresponding value of turn rate is nearly 140 deg s^{-1}.

Remark. This case represents the standard coordinated turn: the asymmetric wing incidence angles (like ailerons) are used to maintain roll equilibrium, while the left dihedral maintains equilibrium in yaw. The observation that the wing incidence angle is not very large suggests that controlling the wing dihedral angles alone may suffice to maintain the roll and yaw equilibrium across a range of turn rates.

5.6.3. Case 3 ($\theta_L = \theta_R = 0$; variable δ_L; δ_R freed for $\beta = 0$). Consider the third case where the wing incidence is held fixed at zero. The left wing dihedral angle is varied independently, while the right-wing dihedral is scheduled to maintain zero sideslip. This case is presented to show that the wing dihedral angles alone are capable of controlling a turn. Alternately, this case may be viewed as a redundancy to accommodate failures in the mechanism to control wing incidence. Physically, an asymmetric dihedral deflection of the wings leads to an asymmetry in the lift distribution on the two wings which, in turn, leads to rolling as well as yawing moments. The two moments can be controlled independently by choosing the wing dihedral angles appropriately.

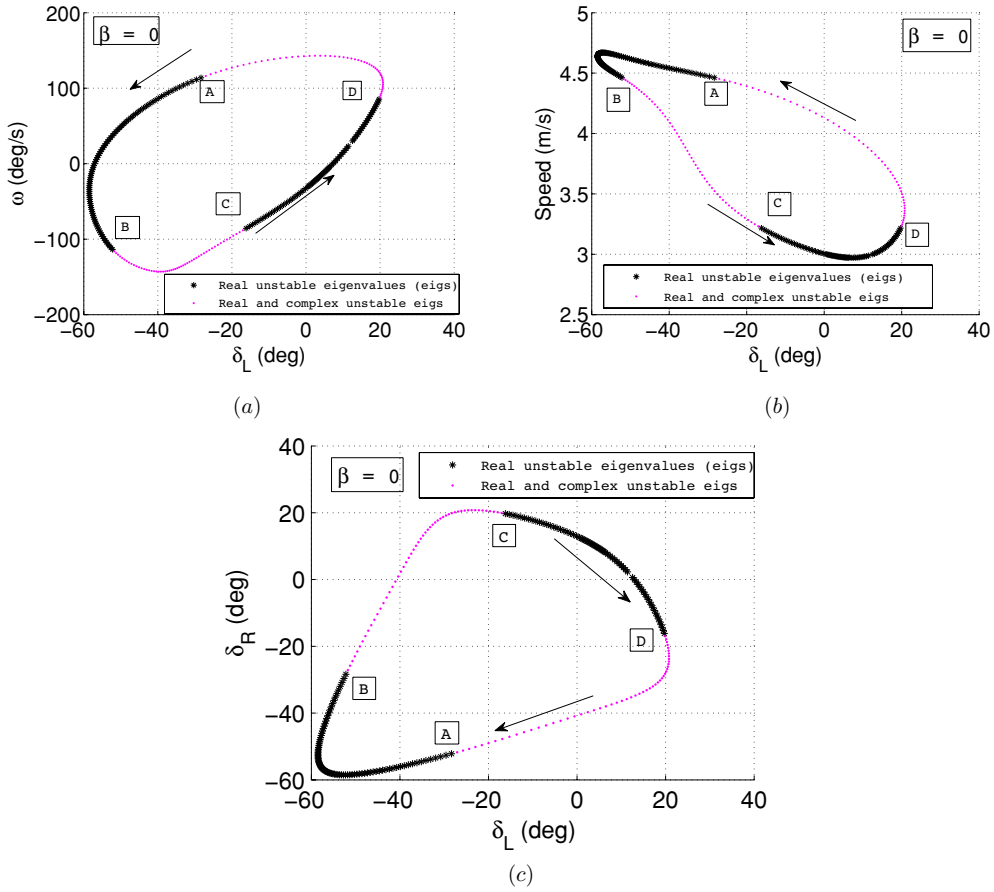

Figure 12. Case 3: coordinated turn trims as functions of the left wing dihedral. The short arrow indicates a reference solution, while the long arrows track ω, V and δ_R as δ_L is varied. Points A, B, C and D are Hopf bifurcations. (a) Turn rate as a function of the left wing dihedral, with $\beta = 0$. (b) Flight speed as a function of the left wing dihedral, with $\beta = 0$. (c) Right-wing dihedral required to maintain $\beta = 0$.

Figures 12(a)–(c) plot the turn rate, flight speed and the right-wing dihedral angle, respectively, as a function of the left wing dihedral. The equilibrium surface topology is very different from cases 1 and 2. The equilibrium surface is a closed loop. The left- and right-wing dihedral angles can be set to achieve fairly large turn rates, as evident in figure 12(a). Interestingly enough, a larger anhedral (negative dihedral) deflection is required of both wings as compared to the upward dihedral deflection. It is helpful to recall that a black asterisk '$*$' denotes an equilibrium with positive real eigenvalues, while a magenta filled circle ($\cdot$) denotes an equilibrium with positive real as well as positive complex conjugate eigenvalues. It follows that points A, B, C and D in figure 12 are Hopf bifurcations. In segments AD and BC, the aircraft demonstrates oscillatory behaviour with large angular rates, as in oscillatory spins. On the other hand, it diverges from segments AB and CD to *equilibrium* steady states not shown in figure 12.

Remark. This case serves as a useful pointer to control design. The aircraft would perform routine turns in the close vicinity of trims between the Hopf bifurcations C and D, which have a divergent yaw instability. When the trims between C and D are stabilized by linear yaw rate feedback, the following situation is observed [43]: the aircraft can be made to enter a rapid turn, but the same feedback law does not help it recover to straight and level flight. Instead, the aircraft performs limit cycle oscillations, as one would expect from the existence of Hopf bifurcations C and D. Aircraft similar to the one considered in this paper would exhibit similar nuances. Instead of a linear yaw rate feedback, a nonlinear yaw rate feedback is required to recover the aircraft to stable, wings level flight from a turn.

5.6.4. Case 4 (variable θ_L, $\theta_R = -\theta_L$; δ_L and δ_R freed for $\beta = 0$ and constant V). Consider the fourth case, a turn where the flight speed is held constant at an arbitrarily chosen value of $V = 3.0\,\mathrm{m\,s^{-1}}$ and the sideslip is regulated at zero. As in the first two cases, the wing incidence is varied as the independent parameter, while the two dihedral angles are freed to maintain the flight speed and the sideslip at their respective desired values. Figure 13(a) plots the turn rate as a function of the wing incidence. It is apparent that the wing incidence is much smaller than in figure 10, and the turn rate does not increase monotonically with wing incidence. Instead, the equilibria trace a figure-of-eight in figure 13(a) which

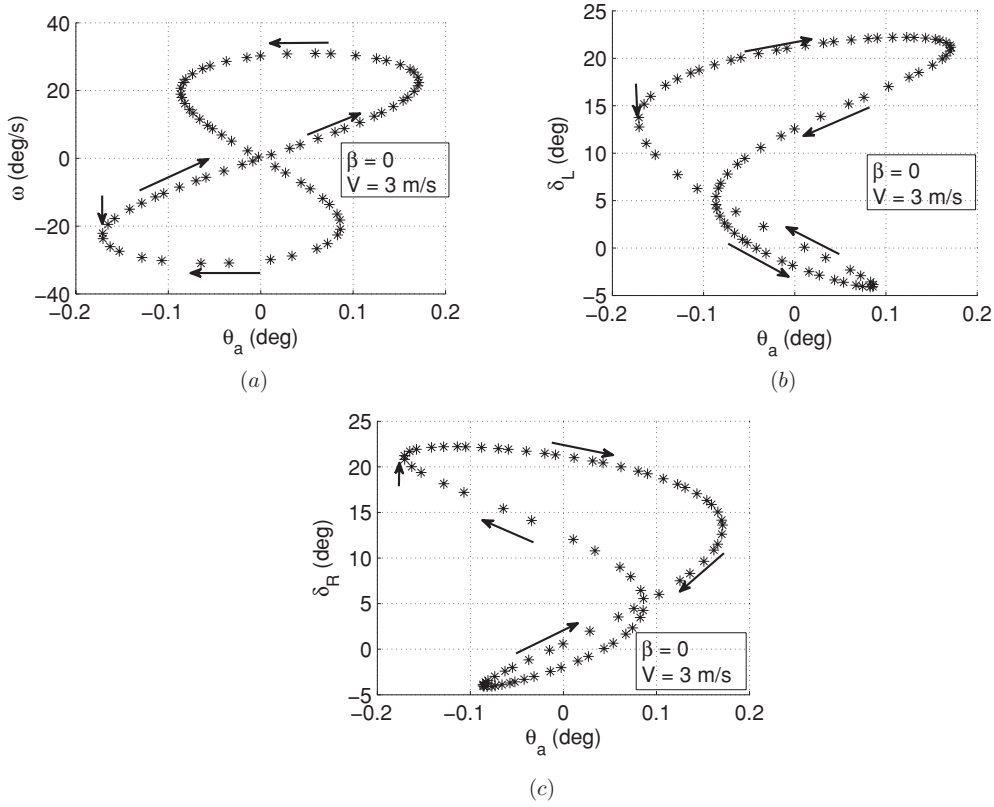

Figure 13. Case 4: coordinated turn trims with left- and right-wing dihedrals varied asymmetrically. Each plot carries two arrows. The short arrow denotes a reference solution, while the long arrow helps track the variation of the turn rate and δ_R starting from the reference solution. (*a*) Turn rate as a function of the anti-symmetric wing incidence with constraints $\beta = 0$ and $V = 3\,\mathrm{m\,s^{-1}}$. (*b*) Left wing dihedral as a function of the anti-symmetric wing incidence with constraint $\beta = 0$ and $V = 3\,\mathrm{m\,s^{-1}}$. (*c*) Right-wing dihedral required to maintain $\beta = 0$ and $V = 3\,\mathrm{m\,s^{-1}}$.

limits the maximum attainable turn rate while, simultaneously, giving rise to multiple equilibrium solutions for a given value of wing incidence. All the equilibrium solutions are observed to be unstable. Figures 13(*b*) and (*c*) plot the left- and right-wing dihedral angles as functions of the wing incidence. The short arrow on each plot indicates a reference solution, and the long arrows help track ω, δ_L and δ_R as the wing incidence is varied. It is interesting to note that the wing dihedral angles become the primary drivers of the turn rate, while the wing incidence plays a secondary role in a coordinated turn at a constant speed. Figure 14 is a 3D plot of the turn rate and the wing dihedral angles and presents a clearer picture of the equilibrium surface topology. The projections of the closed curve in figure 14 onto the ω–δ_L and δ_L–δ_R planes are similar to figures 12(*a*) and (*c*).

Aircraft stability and performance are sensitive to the flight speed chosen for the turn which is, in turn, governed by the elevator deflection. In the above case, for example, in order to perform steady turns at $2.8\,\mathrm{m\,s^{-1}}$ instead of $3\,\mathrm{m\,s^{-1}}$, the elevator deflection has to be increased beyond the previous value of -11.4 deg. The elevator was fixed at -13.7 deg (-0.24 rad) and steady turn trims were computed. Figure 15 shows the turn rate as a function of wing incidence when the dihedral angles on the two wings are scheduled to maintain the flight speed at $2.8\,\mathrm{m\,s^{-1}}$ and regulate the sideslip.

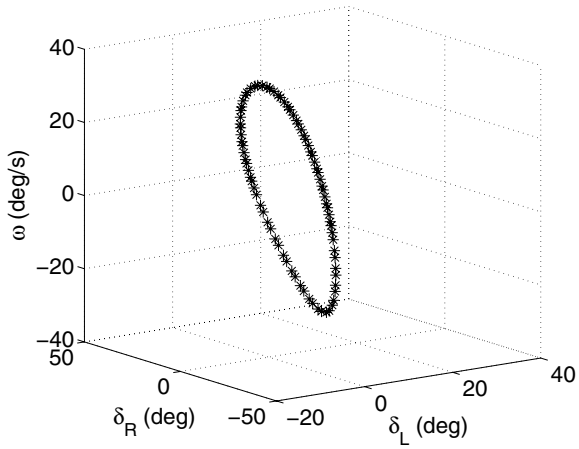

Figure 14. 3D plot of the turn rate and the wing dihedral angles when the sideslip is held fixed at 0 and the flight speed at $3.0\,\mathrm{m\,s^{-1}}$.

Remark. Plots showing the dihedral angle variation are not included for brevity. A comparison of figures 13(*a*) and 15 shows that the maximum turn rate increases significantly when a lower flight speed is maintained. Furthermore, some of the turn equilibria are now unstable with a pair of positive complex conjugate eigenvalues. This could result, possibly, in

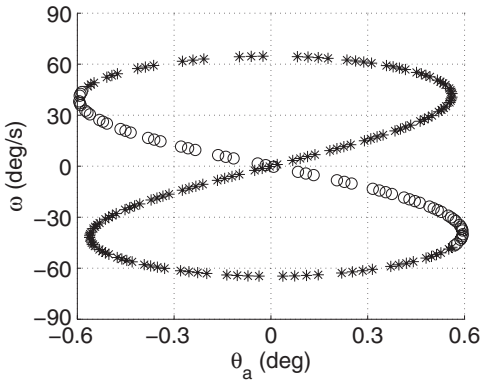

Figure 15. Turn rate as a function of anti-symmetric wing incidence with the constraints $\beta = 0$ and $V = 2.8\,\mathrm{m\,s^{-1}}$. Recall that asterisks '$*$' and empty circles '$\circ$' denote equilibria where all eigenvalues with positive real parts are real and complex conjugate, respectively.

an oscillatory behaviour with the resultant motion resembling a spin owing to the significant turn rates.

6. Experimental results and generalizations

The ideas presented in this paper are being validated experimentally. In this section, some results obtained during open loop studies have been presented. Experiments were performed on Plantraco's Kolibri Pocket Plane (see figures 16(*a*) and (*b*)). The aircraft has a wing span of 220 mm and weighs approximately 5 g. The wing camber is negligible, which means that $C_{\mathrm{m_{ac}}} \approx 0$. Therefore, increasing the dihedral on the left wing relative to the right wing creates a positive yawing moment and vice versa ($\zeta > 0$ in (27)).

The aircraft wings were modified so that their dihedral could be changed *a priori*. Ailerons were added as substitutes for wing incidence, and the vertical tail was duly removed. The aircraft was seen to possess a significantly large L/D ratio. Ballast mass was added to the aircraft to rein in its tendency to accelerate and pull up. Spoilers were added on the inboard section of the wing to improve phugoid damping. Experiments were performed with the elevator set to $\delta_e = -10\,\mathrm{deg}$. The aircraft position was measured directly using VICON and the sampling frequency was set to 100 Hz. The velocities and the heading angles were derived from the position measurements using the finite difference method. For each aircraft configuration, four flights were conducted and the average values of the observed flight parameters are reported here. For longitudinal studies, the angle of attack was approximated as the difference between the body pitch angle and the flight path angle. Even with the added mass and spoilers, the phugoid motion did not damp out sufficiently within the available experimental space for small values of the wing dihedral. Therefore, the mean values of the flight parameters, as the expected steady state values, were noted down.

6.1. Symmetric configuration

The purpose of the experiments with a symmetric configuration was to verify, qualitatively, the results in figure 8. Figures 17(*a*)–(*c*) show the flight speed, angle of attack and flight path angle as a function of the wing dihedral. Flight tests at small values of the dihedral were precarious, because of the tendency of the aircraft to depart into a spiral. Nevertheless, the velocity and the flight path angle trends (also shown by a quadratic fit) match those predicted by the theoretical analysis in the preceding section. The angle of attack increases almost linearly as the dihedral angle is increased from 20 deg to 55 deg. The angle of attack behaviour is seen to deviate substantially from the linear trend for $\alpha < 20\,\mathrm{deg}$ due to the truant dynamics of the aircraft. Consequently, no attempt was made to fit a low order polynomial curve to the angle of attack data.

6.2. Lateral-directional motion

The turning performance of the aircraft was calculated for different values of the aileron deflection. The aircraft,

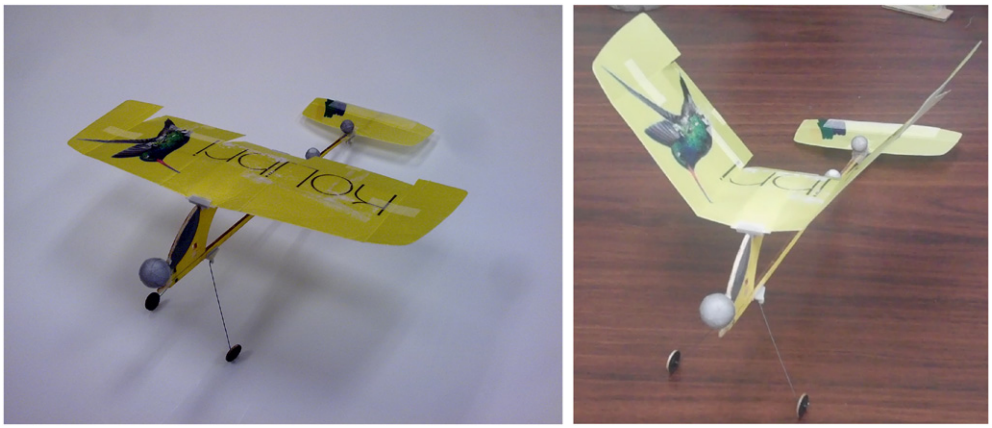

(*a*) (*b*)

Figure 16. The Plantraco Kolibri Pocket Plane, used for experiments described in the paper. (*a*) The aircraft with wing dihedral set to zero. (*b*) The aircraft with its wings raised to a dihedral of 55 deg.

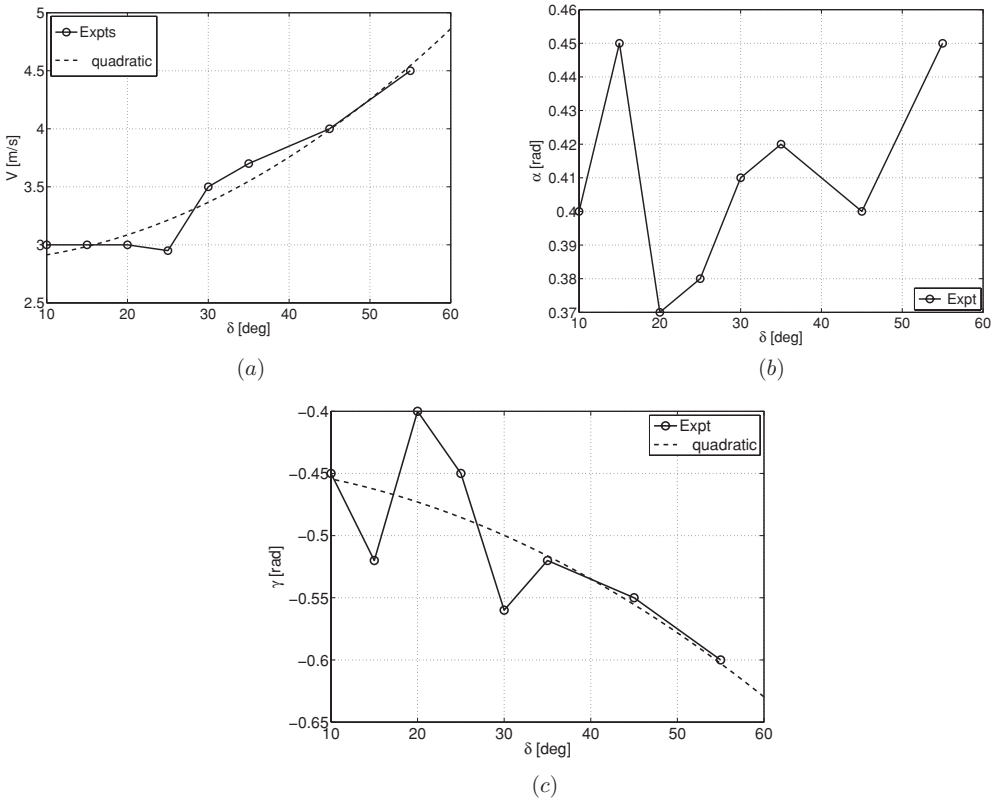

Figure 17. Steady state values of the longitudinal flight parameters as functions of the wing dihedral. (*a*) Flight speed as a function of the dihedral. (*b*) Angle of attack as a function of the dihedral. (*c*) Flight path angle as a function of the wing dihedral.

Table 4. A summary of the turning performance. The aileron deflection has been denoted by δ_a. The negative sign implies that the aircraft rolls to the left.

δ_a (deg)	δ_R (deg)	δ_L (deg)	V (m s^{-1})	ω (deg s^{-1})	β (deg)
−5	5	−5	3.6	104.6	4.6
	10	−5	3.74	133.5	8.02
	10	−10	3.8	154.7	13.2
−10	10	−10	3.5	160.4	−4.6
	15	−10	3.5	160.4	11.46

however, was seen to be unstable, similar to that in the experiments with a symmetric configuration. In fact, an oscillatory spin-like motion was observed during a few experiments. The results of the experiments have been tabulated in table 4. The aileron deflection has been denoted by δ_a.

The aircraft was seen to possess a very poorly damped transient performance. Consequently, the values in table 4 are approximate, in that they are obtained as the expected steady state solutions. Beyond $\delta_a = -15$ deg, the aircraft became unstable ruling out any meaningful turning experiments in the open loop. The data presented in table 4 is, nevertheless, instructive in its own right.

For $\delta_a = -5$ deg, note that the aircraft sideslip increases as δ_R–δ_L is increased. The desired coordinated turn would hence occur when δ_L is just less than 5 deg. The flight speed is almost constant, which matches the expectations from the earlier trim analysis. The aircraft turn rate increases as δ_R–δ_L increase due of the consequent increase in the side force.

For $\delta_a = -10$ rad, the sideslip is zero when $\delta_L = -10$ deg, and δ_R is between 10 and 15 deg. Note that the turn rate and flight speed are almost constant. Therefore, a part of the increased sideforce is lost in compensating for the sideslip. It is interesting that even such sparse and crude, albeit carefully chosen, data can be useful for predicting the optimal dihedral combination for coordinated turns.

6.3. Generalizations and trade-offs

The results in the aforementioned sections can be readily generalized to other similar aircraft. Although the numerical results were presented only for an aircraft based on the Vapor, it will be appreciated that they are based on a fundamental underlying concept whose validity does not depend on the aircraft to which it is applied. One could expect some quantitative changes with aircraft geometry.

If the aircraft CG is located ahead of the wing AC, an asymmetric dihedral or an asymmetric force distribution on the wing would generate a yawing moment as explained in section 5.1. From figure 5, it follows that the yawing moment would be adverse in nature. At the same time, placing the CG ahead of the wing AC would increase the moment arm of the horizontal tail which would, in turn, improve the longitudinal performance and stability. Consider an aircraft rolling to the

right. In this case, a positive proverse yawing moment can be obtained by deflecting the right wing upwards. Moreover, an upward deflection of the right wing leads to a proverse contribution from $C_{m_{ac}}$ as well. However, deflecting the right wing upwards would reduce the net side force. The reduction in side force would be beneficial while performing a pure roll, but it would be undesirable if the aircraft is rolling while turning to the right.

Contrary to the last paragraph, consider the configuration where the wing AC is ahead of the CG. This is the configuration which has been analysed in detail in this paper. Recall (27):

$$\zeta = \frac{S_w l_w}{S_t l_t}\alpha_w + \frac{S_w c}{S_t l_t}\frac{C_{m_{ac}}}{C_{L_\alpha}}. \tag{34}$$

It is evident that a negative wing $C_{m_{ac}}$, which results from a positive wing camber, has a detrimental effect on the dihedral effectiveness ration ζ. One may be tempted to consider minimizing the camber to improve ζ, as suggested in section 5.1. However, note that α_w depends on the wing camber as well—it reduces with a reduction in camber. For a wing with no camber, $\alpha_w = \alpha$, the geometric angle of attack, and $C_{m_{ac}} = 0$. Therefore, the camber value could be chosen during design to maximize ζ.

The yawing moment that arises from an asymmetry in the wing configuration or aerodynamic force distribution can be traced to three sources. The primary source of yawing moment is the side force, illustrated in figure 5. The second source is $C_{m_{ac}}$, which was discussed in the last paragraph. The third source, which has not been discussed so far, is drag. A positive roll rate increases the angle of attack on the right wing, and reduces that of the left wing. This leads to a higher drag on the right wing which contributes a proverse yawing moment. This stabilizing effect of drag is well known. Interestingly, increasing the left wing dihedral enhances the proverse yaw moment by further reducing the angle of attack, and consequently the drag, on the left wing. This effect would be enhanced at low Reynolds numbers, where the coefficient of drag increases substantially due to viscous effects. When the wing AC is behind the CG, the right-wing dihedral would be increased to provide the necessary yawing moment, which would detract from the proverse contribution of drag.

It is evident from the discussion that the choice of the CG location involves a trade-off between the longitudinal and lateral performance. Indeed, there are several merits in placing the CG behind the wing aerodynamic centre, contrary to regular fixed wing aircraft with a vertical tail where the CG should be placed as far ahead as possible to improve the longitudinal as well as lateral performance.

7. Conclusions

The ultimate goal of this work is to develop MAVs that can mimic or exceed the agile manoeuvres of birds. This paper laid the flight mechanic foundations for one such tailless aircraft concept equipped with articulated wings. The results of this paper, although valid in principle for all aircraft regardless of their size, are particularly relevant to MAVs because their size and speed make the articulated wing-based control scheme practically realizable. Flapping wing aircraft can benefit from the control scheme described in this paper because flapping wing aircraft are equipped with the necessary actuators, and no additional actuation mechanisms are required. In this paper, the effect of wing dihedral on the performance and stability of articulated wing aircraft was examined in detail. Wing dihedral, together with the horizontal tail, can be used to control the flight path angle (or the angle of attack) *and* the flight speed independently for a range of flight speeds. Asymmetric dihedral deflection was demonstrated as an effective yaw control mechanism for agile MAVs. It was shown that the aircraft sideslip can be regulated effectively during rapid turns using the wing dihedral. Using the left- and right-wing dihedral angles independently and simultaneously, it is possible to achieve coordinated turns across a wide range of turn rates while keeping the flight speed fixed. At the same time, the control effectiveness of dihedral for yaw control was shown to be highly sensitive to the angle of attack and the angular rates which would make automatic control design a challenging task, and increase the possibility of compounding the inherent instability of the dynamics. The ideas presented in this paper are being validated experimentally on a tailless MAV. Some preliminary experimental results demonstrated the qualitative validity of trim predictions from the numerical analysis. The future work on the larger problem of developing highly agile MAVs would focus on (a) the development of aggressive control laws which incorporate asymmetric dihedral actuation, and (b) incorporating the effects of wing flexibility and honing them to improve the manoeuvrability.

Acknowledgment

The authors thank the anonymous reviewer for his helpful comments and suggestions which helped improve the paper to its present form. This project was supported by the Air Force Office of Scientific Research (AFOSR) under the Young Investigator Award Program (grant no FA95500910089) monitored by Dr Willard Larkin. The original problem was posed by Dr Gregg Abate (AFRL). This paper also benefitted from stimulating discussions with Mr Johnny Evers (AFRL). Dr Animesh Chakravarthy (Wichita State University) provided useful feedback and comments from the very inception of this work, and helped to refine the paper to the present state. Daniel Uhlig at UIUC provided the aerodynamic data in figure 4 as well as the approximations in (25). The authors also thank undergraduate research assistants James Holtman, Joseph Kim, Andrew Meister, Daniel Park and Jonathan Yong for their efforts with the experiments.

References

[1] Ol M, Parker G, Abate G and Evers J 2008 Flight controls and performance challenges for MAVs in complex environments *AIAA Paper* 2008-6508

[2] Mueller T J 2001 *Fixed and Flapping Wing Aerodynamics for Micro Air Vehicle Applications (Progress in Aeronautics and Astronautics* vol 195*)* (Reston, VA: AIAA)

[3] Chung S-J and Dorothy M 2010 Neurobiologically inspired control of engineered flapping flight *J. Guid. Control Dyn.* **33** 440–53

[4] Bourdin P, Gatto A and Friswell M 2008 Aircraft control via variable cant-angle winglets *J. Aircr.* **45** 414–23

[5] Gatto A, Bourdin P and Friswell M 2010 Experimental investigation into articulated winglet effects on flying wing surface pressure aerodynamics *J. Aircr.* **47** 1811–6

[6] Costello M and Webb A 2008 Wing articulation of micro air vehicles to reduce gust sensitivity *AIAA Paper* 2008-6712

[7] Wickenheiser A and Garcia E 2006 Longitudinal dynamics of a perching aircraft *J. Aircr.* **43** 1386–92

[8] Wickenheiser A and Garcia E 2008 Optimization of perching maneuvers through vehicle morphing *J. Guid. Control Dyn.* **31** 815–23

[9] Reich G W, Wojnar O and Albertani R 2009 Aerodynamic performance of a notional perching MAV design *AIAA Paper* 2009-63

[10] Stenfelt G and Ringertz U 2009 Lateral stability and control of a tailless aircraft configuration *J. Aircr.* **46** 2161–3

[11] Stenfelt G and Ringertz U 2010 Yaw control of a tailless aircraft configuration *J. Aircr.* **47** 1807–10

[12] Shtessel Y, Buffington J and Banda S 2002 Tailless aircraft flight control using multiple time scale reconfigurable sliding modes *IEEE Trans. Control Syst. Technol.* **10** 288–96

[13] Obradovic B and Subbarao K 2010 Modeling of dynamic loading of morphing wing aircraft *AIAA Paper* 2010-8236

[14] Sachs G and Holzapfel F 2007 Flight mechanic and aerodynamic aspects of extremely large dihedral in birds *AIAA Paper* 2007-46

[15] Sachs G 2007 What can be learned from unique lateral-directional dynamics properties of birds for mini-aircraft *AIAA Paper* 2007-6311

[16] Sachs G 2007 Why birds and miniscale airplanes need no vertical tail *J. Aircr.* **44** 1159–67

[17] Tran D and Lind R 2010 Parametrizing stability derivatives and flight dynamics with wing deformation *AIAA Paper* 2010-8227

[18] Goman M G, Zagaynov G I and Khramtsovsky A V 1997 Application of bifurcation theory to non-linear flight dynamics problems *Prog. Aerosp. Sci.* **33** 539–86

[19] Lowenberg M 2002 Bifurcation and continuation method *Advanced Techniques for Clearance of Flight Control Laws* ed M Selier (Berlin: Springer) pp 88–106

[20] Paranjape A A, Sinha N K and Ananthkrishnan N 2008 Use of bifurcation and continuation methods for aircraft trim and stability analysis—a state-of-the-art *J. Aerosp. Sci. Technol.* **60** 1–12

[21] Thomas A L R and Taylor G K 2001 Animal flight dynamics: I. Stability in gliding flight *J. Theor. Biol.* **212** 399–424

[22] Ramsey J A, Ratliff R T, Wise K A and Lavretsky E 2009 Departure resilient control for autonomous air vehicles *Proc. 2009 American Control Conf.* pp 5386–91

[23] Chakravarthy A, Paranjape A A and Chung S-J 2010 Control law design for perching an agile MAV with articulated wings *AIAA Paper* 2010-7934

[24] Azuma A 2006 *The Biokinetics of Flying and Swimming* 2nd edn (Reston, VA: AIAA)

[25] Uhlig D, Sareen A, Sukumar P, Rao A and Selig M 2010 Determining aerodynamic characteristics of a micro air vehicle using motion tracking *AIAA Paper* 2010-8416

[26] Paranjape A A and Ananthkrishnan N 2005 Aircraft level turn performance, including stability constraints, using EBAC method *AIAA Paper* 2005-5898

[27] Keller H B 1977 Numerical solution of bifurcation and nonlinear eigenvalue problems *Applications of Bifurcation Theory* ed P Rabinowitz (New York: Academic)

[28] Doman D, Oppenheimer M and Sigthorsson D 2010 Wingbeat shape modulation for flapping-wing micro-air-vehicle control during hover *J. Guid. Control Dyn.* **33** 724–39

[29] Wright J R and Cooper J E 2007 *Introduction to Aircraft Aeroelasticity and Loads (Aerospace Series)* (Chichester: Wiley)

[30] Johnson W 1980 *Helicopter Theory* (New York: Dover)

[31] McMillan O J, Schwind R G, Nielsen J N and Dillenius M F E 1977 Rolling moments in a trailing vortex flow field *NEAR TR 129*, also *NASA CR-151961*

[32] Jr Poppen A P 1985 A method for estimating the rolling moment due to spin rate for arbitrary planform wings *NASA TM-86365*

[33] Pamadi B N and Jr Taylor L W 1984 Estimation of aerodynamic forces and moments on a steadily spinning airplane *J. Aircr.* **21** 943–54

[34] Pamadi B N 1998 *Performance, Stability, Dynamics, and Control of Airplanes (AIAA Education Series)* (Reston, VA: AIAA)

[35] Stone R H 2008 Aerodynamic modeling of the wing-propeller interaction for a tail-sitter unmanned air vehicle *J. Aircr.* **45** 198–210

[36] Keller J D, McKillip Jr R M and Wachspress D A 2008 Physical modeling of aircraft upsets for real-time simulation applications *AIAA Paper* 2008-6205

[37] Keller J D, McKillip Jr R M and Kim S 2009 Aircraft flight envelope determination using upset detection and physical modeling methods *AIAA Paper* 2009-6259

[38] Selig M S 2010 Modeling full-envelope aerodynamics of small UAVs in realtime *AIAA Paper* 2010-7635

[39] Selig M S 2010 Modeling propeller aerodynamics and slipstream effects on small UAVs in realtime *AIAA Paper* 2010-7938

[40] McCormick B W 1994 *Aerodynamics, Aeronautics and Flight Mechanics* 2nd edn (New York: Wiley)

[41] Borglund D and Kuttenkeuler J 2002 Active wing flutter suppression using a trailing edge flap *J. Fluids Struct.* **16** 271–94

[42] Paranjape A A, Chakravarthy A, Chung S-J and Hilton H H 2010 Performance and stability of an agile MAV with flexible articulated wings *AIAA Paper* 2010-7937

[43] Paranjape A A, Kim J and Chung S-J 2011 Experimental demonstration of perching by a tailless articulated wing MAV *Proc. AIAA Guidance Navigation and Control Conference 2011 (Portland, OR)* at press

[44] Liefer R K, Valasek J, Eggold D P and Downing D R 1992 Fighter agility metrics, research and test *J. Aircr.* **29** 452–7